

**The Rotating Outflow, Envelope and Disk
in Class-0/I protostar [BHB2007] #11 in the Pipe Nebula**

C. Hara

The University of Tokyo¹ / National Astronomical Observatory of Japan²

c.hara@nao.ac.jp

Y. Shimajiri

Nobeyama Radio Observatory³ / National Astronomical Observatory of Japan²

T. Tsukagoshi

Ibaraki University⁴

Y. Kurono, K. Saigo

National Astronomical Observatory of Japan²

F. Nakamura

National Astronomical Observatory of Japan²

M. Saito

National Astronomical Observatory of Japan² / Joint ALMA Observatory⁵

David Wilner

Harvard Smithsonian Center for Astrophysics⁶

and

R. Kawabe

National Astronomical Observatory of Japan² / Joint ALMA Observatory⁵

Received _____; accepted _____

Not to appear in Nonlearned J., 45.

¹7-3-1 Hongo Bunkyo, Tokyo 113-0033, Japan

²2-21-1 Osawa Mitaka, Tokyo 181-0015, Japan

³462-2 Nobeyama Minamimaki, Minamisaku District, Nagano Prefecture 384-1305, Japan

⁴2-1-1 Bunkyo Mito, Ibaraki Prefecture 310-8512, Japan

⁵Alonso de Cordova 3107 Vitacura, Satiago 763 0355, Chile

⁶Center for Astrophysics, 60 Garden Street, Cambridge, MA 02138

ABSTRACT

We present the results of observations toward a low-mass Class-0/I protostar, [BHB2007]#11 (afterwards B59#11) at the nearby ($d=130$ pc) star forming region, Barnard 59 (B59) in the Pipe Nebula with the Atacama Submillimeter Telescope Experiment (ASTE) 10 m telescope ($\sim 22''$ resolution) in CO(3–2), HCO⁺, H¹³CO⁺(4–3), and 1.1 mm dust-continuum emissions. We also show Submillimeter Array (SMA) data in ¹²CO, ¹³CO, C¹⁸O(2–1), and 1.3 mm dust-continuum emissions with $\sim 5''$ resolution. From ASTE CO(3–2) observations, we found that B59#11 is blowing a collimated outflow whose axis lies almost on the plane of the sky. The outflow traces well a cavity-like structure seen in the 1.1 mm dust-continuum emission. The results of SMA ¹³CO and C¹⁸O(2–1) observations have revealed that a compact and elongated structure of dense gas is associated with B59#11, which is oriented perpendicular to the outflow axis. There is a compact dust condensation with a size of 350×180 AU seen in the SMA 1.3 mm continuum map, and the direction of its major axis is almost the same as that of the dense gas elongation. The distributions of ¹³CO and C¹⁸O emission also show the velocity gradients along their major axes, which are considered to arise from the envelope/disk rotation. From the detailed analysis of the SMA data, we infer that B59#11 is surrounded by a Keplerian disk with a size of less than 350 AU. In addition, the SMA CO(2–1) image shows a velocity gradient in the outflow along the same direction as that of the dense gas rotation. We suggest that this velocity gradient shows a rotation of the outflow.

Subject headings: stars: formation — ISM: clouds — ISM: radio continuum — ISM: molecules — ISM: individual ([BHB2007]#11)

1. Introduction

Stars are formed through the gravitational collapse of a molecular cloud core, and during the collapse, the system undergoes an increasing density of 20 orders of magnitude. In the course of the gravitational collapse, a core is considered to spin up and eventually a Keplerian disk is formed around a protostar and grows in size during the main accretion phases.

Previous interferometric observations in molecular lines have found evidences of Keplerian disks around protostars in main accretion phases (e.g., Brinch et al. (2007); Lommen et al. (2008); Jørgensen et al. (2009)). These protostars, however, have somewhat high bolometric temperatures ($T_{\text{bol}}=238$ K, 391 K, 351 K, and 310 K for L1489-IRS, Elias 29, IRS 63, and IRS 43, respectively) indicating that these are more evolved protostars than the Class-0 phase, and the initial conditions of disks have not been revealed yet. Takakuwa et al. (2012) and Lee (2010) also found Keplerian disks around Class-I protobinary systems in earlier evolutionary phases (L1551NE; $T_{\text{bol}}=91$ K, HH111; $T_{\text{bol}}=78$ K). There are, however, few samples of Keplerian disks observationally identified around protostars in the early phases.

The Barnard 59 (B59) is an irregularly shaped dark cloud sitting at the end of the Pipe Nebula. Here, we adopt a distance to B59 of 130_{-20}^{+13} pc (Lombardi et al. 2006), which is most-commonly used in the previous studies of the Pipe Nebula. Although Alves & Franco (2007) proposed a distance of 145 ± 16 pc, our adopted distance is consistent within uncertainties of their analyses. It should be noted that masses estimated in this paper have uncertainties of ~ 20 % according to an uncertainty of the distance of ~ 10 %. Onishi et al. (1999) carried out mapping observations toward the Pipe Nebula in CO(1–0) and C¹⁸O(1–0) lines, and detected 14 C¹⁸O dense cores. A CO(1–0) outflow was detected only at B59, suggesting that B59 is an only active star-forming region in the Pipe Nebula

(Onishi et al. 1999). Spitzer observations have revealed 20 low-mass young stellar objects (YSOs), and suggest that the star formation efficiency of the cluster is $\sim 20\%$ (Brooke et al. 2007). More detailed photometry at MIPS bands has revealed that there are 15 low-mass YSOs in the 0.3×0.3 pc area (Forbrich et al. 2009). The median stellar age of B59 has been estimated to be $2.6_{-2.6}^{+4.1}$ Myr (Covey et al. 2010). [BHB2007]#11 (hereafter, B59#11) is a deeply embedded low-mass protostar in the B59 region and classified as a Class-0/I object, which is in the transition phase from Class-0 to I with a bolometric temperature of 70 K (Brooke et al. 2007) and considered to be younger than the B59 median stellar age of ~ 2.6 Myr. It is the strongest $70 \mu\text{m}$ emission source in the B59 region and has a bolometric luminosity of $2.2 \pm 0.3 L_{\odot}$. Brooke et al. (2007) detected extended IRAC $3.6 \mu\text{m}$ and $4.5 \mu\text{m}$ emissions on the northeast of B59#11. These structures imply that a molecular outflow ejected from B59#11 creates a cavity. Riaz et al. (2009) analyzed these extended nebulosities and have suggested that the inclination angle of the outflow ejected from B59#11 is 53° - 59° . Duarte-Cabral et al. (2012), however, found that the outflow associated with B59#11 is ejected almost in the plane of the sky from observations of molecular outflows in the CO(3–2) line. Riaz et al. (2009) also pointed out that B59#11 is building up a weakly bounded binary system with 2M17112255-27243448 (hereafter, B59#11SW; the apparent separation is ~ 1300 AU).

We present the results of ASTE 10 m telescope observations in CO(3–2), HCO⁺, H¹³CO⁺(4–3), and 1.1 mm dust-continuum emissions and SMA observations in ¹²CO, ¹³CO, C¹⁸O(2–1), and 1.3 mm dust-continuum emissions toward the low-mass Class-0/I protostar, B59#11, which is thought to be one of the good targets for investigating the disk formation in the early protostellar evolution. First, we present the details of our ASTE observations and SMA data reductions in Section 2. In Section 3, we show the results of ASTE and SMA observations and derive the physical properties of the outflow and the dense gas associated with B59#11. In Section 4, we discuss the possibility that B59#11

has a rotationally supported disk and a rotating outflow. Finally, we summarize our main conclusions in Section 5.

2. Observations

2.1. AzTEC/ASTE Observations

We carried out 1.1 mm dust-continuum observations toward the B59 region with the AzTEC camera (Wilson et al. 2008) mounted on the ASTE 10 m telescope (Ezawa et al. 2004; Kohno et al. 2004) located at Pampa la Bola (altitude=4800 m), Chile. The observations were performed in the period October 17 to 31, 2008. The weather conditions during the period were good or moderate, and the typical atmospheric opacity at 225 GHz was in the range of 0.04-0.2. The AzTEC camera mounted on the ASTE telescope is a 144-element bolometric camera and provides us with an angular resolution of $28''$ in full width at half maximum (FWHM)(Wilson et al. 2008). The 1.1 mm continuum observations of B59 were performed as a part of the survey of nearby star forming regions (Kawabe et al. 2013, in preparation). The observations were performed in the raster scan mode toward the $35' \times 35'$ area centered on $(\alpha_{J2000}, \delta_{J2000})=(17^{\text{h}}11^{\text{m}}58^{\text{s}}.57, -27^{\circ}24'27''.86)$. Each field was observed several times with azimuth and elevation scans. The separation among scans was adopted to be $117''$, which is a quarter of the AzTEC field of view (FoV; $\sim 7'.8$). The scanning speed of the telescope was $250'' \text{ s}^{-1}$. In total, 28 individual maps of the entire field with an integration time of 9.4 minutes were taken, and those maps were averaged to produce a final map with a total integration time of 4.4 hours. The telescope pointing was checked every 2 hours by observing quasars, J1924-292 and J1733-130. The derived pointing offsets were linearly interpolated along the time sequence, and the interpolated pointing offset was applied to each target map. The pointing accuracy of the AzTEC map is estimated to be better than $2''$. The flux scale was calibrated by observing the planet

Uranus twice per night, and we measured the flux conversion factor (FCF) from optical loading value (in Watts) to the source flux (in Jy beam⁻¹) for each detector element. A principal component analysis (PCA : Scott et al. (2008)) cleaning method was applied to remove atmospheric noise. Details of the flux calibration are described by Wilson et al. (2008) and Scott et al. (2008). Since the PCA method does not have sensitivity to extended sources, we applied an iterative mapping method (FRUIT : Liu et al. (2010); Shimajiri et al. (2011)) to recover the extended components. The noise level is ~ 6 mJy beam⁻¹ in the central region and ~ 7 mJy beam⁻¹ in the outer edge. The effective beam size of $\sim 36''$ is estimated from Gaussian fitting of the point source in the map. We also use the CLEANed image of PCA map to estimate parameters for point sources, in order to avoid the contamination due to the extended emissions seen in the FRUIT map. The PCA cleaning method produced a negative hole around the point-like source, due to the point-spread function (PSF) (see Tsukagoshi et al. 2011). A CLEANed map was made by subtracting the measured PSF from emission via the CLEAN algorithm and by convolving the Gaussian beam with the FWHM of $35''$ to CLEAN components. Details are described in Kawabe et al. (2013, in preparation).

2.2. ASTE ¹²CO(3–2), HCO⁺(4–3), and H¹³CO⁺(4–3) Line Observations

We observed the ¹²CO($J=3-2$; 345.796 GHz), HCO⁺($J=4-3$; 356.734 GHz), and H¹³CO⁺($J=4-3$; 346.998 GHz) transitions toward the B59 region during May in 2011 to January in 2012. The half-power beam width of the ASTE telescope is $\sim 22''$ at the CO(3–2) frequency. The typical system noise temperature with the 345 GHz SIS heterodyne receiver was 300-600 K during our observations. The temperature scale was determined by the chopperwheel method (Kutner & Ulich 1981), which provides us with the antenna temperature corrected for the atmosphere attenuation. As a back end, we used four

sets of a 1024 channel auto-correlator, which provided frequency resolution of 125 kHz, corresponding to $\sim 0.1 \text{ km s}^{-1}$ at the $\text{HCO}^+(4-3)$ and $\text{H}^{13}\text{CO}^+(4-3)$ frequencies. The on-the-fly (OTF) mapping technique was used to construct a map covering an area of $15' \times 11'$ (corresponding to $0.6 \times 0.4 \text{ pc}$) in $\text{CO}(3-2)$ emission. In addition, the position-switching mode was used to construct two smaller maps of H^{13}CO^+ and HCO^+ emission, the first one with an area of $60' \times 60'$ (corresponding to $0.04 \times 0.04 \text{ pc}$), and the second one with an area of $80' \times 80'$ (corresponding to $0.05 \times 0.05 \text{ pc}$). In both maps, a grid separation of $20''$ was used. The telescope pointing was checked every 2 hours by five-point scans of the point-like $^{12}\text{CO}(J = 3-2)$ emission from Waql ($\alpha_{J2000.0}, \delta_{J2000.0}$) = ($19^{\text{h}}15^{\text{m}}23^{\text{s}}.35$, $-07^{\circ}02'50''.3$), and IRAS 16594-4656 ($\alpha_{J2000.0}, \delta_{J2000.0}$) = ($17^{\text{h}}03^{\text{m}}10^{\text{s}}.03$, $-47^{\circ}00'27''.68$). The pointing errors were measured to be from $1''$ to $2''$ during the observations. A main beam efficiency is 50%. We subtracted linear baselines from the OTF spectra, then we convolved the maps with a spherical function and resampled them onto a $7''.5$ grid. Since the telescope beam size is $22''$, the effective FWHM resolution in the restored images is $27''$. The scanning effect was minimized by combining scans along the R.A. and Decl. directions, using the PLAIT algorithm developed by Emerson & Graeve (1988). The typical rms noise level in the final image is 1.5 K in T_{A}^* at a velocity resolution of 0.1 km s^{-1} .

2.3. SMA Data Reduction

We also processed the archival data from the SMA observations of [BHB2007]#11 and constructed both the continuum and spectral line images. The 1.3 mm continuum emission was observed with SMA in the compact configuration (7 antennas). The minimum and maximum baselines are $7 \text{ k}\lambda$ and $50 \text{ k}\lambda$, respectively. $^{12}\text{CO}(J=2-1; 230.538 \text{ GHz})$, $^{13}\text{CO}(J=2-1; 220.399 \text{ GHz})$, and $\text{C}^{18}\text{O}(J=2-1; 219.560 \text{ GHz})$ emissions were observed simultaneously with the 1.3 mm continuum emission. The raw data were calibrated using

the MIR package for IDL that was developed for reductions of SMA data based on the Owens Valley Radio Observatory MMA package (Scoville et al. 1993). In the reduction, visibilities with clearly deviating phase and/or amplitudes were flagged. Observations of the calibrator NRAO530 and J1924-292 were interleaved with the target for complex gain calibration. The passband response was calibrated using a strong source 3C454.3. Absolute flux scale was determined by a bootstrap method with Callisto and should be accurate at the 10% level, by comparison of the quasar fluxes with the SMA calibration database. The phase reference center toward the target is $(\alpha_{J2000.0}, \delta_{J2000.0}) = (17^{\text{h}}11^{\text{m}}23^{\text{s}}.18, -27^{\circ}24'31''.5)$. After the calibrations, final CLEANed images were made using MIRIAD (Sault et al. 1995) with natural uv weighting. The resulting synthesized beam size was $5''.0 \times 2''.8$ (corresponding to 650×360 AU) with a position angle of 31° for the dust-continuum map. The achieved rms noise levels were 12 mJy beam^{-1} for the dust-continuum map and $200 \text{ mJy beam}^{-1}$ for ^{13}CO , C^{18}O , and $\text{CO}(2-1)$ images. The final images were uncorrected for the primary beam attenuation. The details of observations are summarized in Table. 2.

3. Results

3.1. Large Scale Structures of B59

3.1.1. *AzTEC/ASTE 1.1 mm Dust-Continuum Emission*

Figure 1 shows the AzTEC/ASTE 1.1 mm FRUIT image obtained toward the north end of the Pipe Nebula. The image shows two dusty clumps which correspond to Core 1 (i.e., B59) and Core 2 detected in the low spatial resolution $\text{C}^{18}\text{O}(1-0)$ map (Onishi et al. 1999). The clump associated with Core 2 has a filamentary structure ~ 0.6 pc long. In addition, other filamentary structures were also detected in our map. These overall structures are in good agreement with the A_V map produced by infrared observations,

and the 1.2 mm dust-continuum map (Román-Zúñiga et al. 2009, 2012). The B59 clump consists of several dust condensations in 1.1 mm dust-continuum emission. Peak positions of four condensations coincide with positions of YSOs, [BHB2007]#1, #9, #10, and #11 identified in the infrared surveys (Brooke et al. 2007). The dust-continuum emission associated with B59#11 is the strongest in the B59 region, and has a peak intensity of 1.9 Jy beam^{-1} . On the northeast of B59#11, a cavity-like structure $\sim 0.06 \text{ pc}$ long was found to be elongated along the southwest-northeast direction. This feature coincides with the one found in the A_V map (Román-Zúñiga et al. 2009).

The mass of B59 (Core 1), M_{dust} , was derived to be $24 M_{\odot}$ from the 1.1 mm total flux obtained from the FRUIT image, F_{ν} , using

$$M_{\text{dust}} = \frac{F_{\nu} d^2}{\kappa_{\nu} B_{\nu}(T_d)} \quad (1)$$

where we assume that all the 1.1 mm dust-continuum emission arises from the dust and is optically thin. Here, we adopt the mass opacity coefficient, $\kappa_{\lambda} = 0.1(250\mu\text{m}/\lambda)^{\beta} \text{ cm}^2 \text{ g}^{-1}$ (Hildebrand 1983) and $\beta=2$, which is a typical value in the interstellar medium (Knacke & Thomson 1973). For the dust temperature, we adopted $T_d=10 \text{ K}$, which is derived from the observations in NH_3 lines (Rathborne et al. 2008). The estimated mass is in good agreement with that of $22.4 M_{\odot}$ derived by Román-Zúñiga et al. (2009) from the A_V map. The mass of the dusty filament (corresponding to Core 2) is estimated to be $4.3 M_{\odot}$ from the FRUIT map.

The mass of the dust condensation associated with B59#11 is also estimated using Equation 1. Here, we used the CLEANed PCA map in order to avoid the contamination due to the extended emission seen in B59, since CLEANed PCA map is less sensitive to extended emissions than the FRUIT map (see Scott et al. (2008) for PCA and Kawabe et al. (2013, in preparation) for CLEANed PCA). The peak flux density of the dust condensation

associated with B59#11 is obtained to be 1.3 Jy beam^{-1} from the CLEANed PCA map with an effective beam size of $36''$. For optically thin emission, the spectral slope between two frequencies, $\alpha = \frac{\log(F_{\nu_1}/F_{\nu_0})}{\log(\nu_1/\nu_0)}$, will be related to the slope, β , of the dust opacity law, $\kappa \propto \nu^\beta$, as $\alpha \approx \beta + 2$ in the Rayleigh-Jeans limit (Beckwith & Sargent 1991). Using the flux estimated from the SHARC-II $350 \mu\text{m}$ map for a $40''$ aperture of $F_{350\mu\text{m}}=45.2 \text{ Jy}$ (Wu et al. 2007) and $F_{1.1\text{mm}}$ in the AzTEC/ASTE observations, the spectral slope, α , is estimated to be $3.0_{-0.2}^{+0.1}$ and β is estimated to be ~ 1 . The dust temperature is estimated to be $\sim 31 \text{ K}$ by a graybody fit with MIPS $70 \mu\text{m}$ (Brooke et al. 2007), SHARC-II $350 \mu\text{m}$ (Wu et al. 2007), and AzTEC 1.1 mm emissions using $\beta=1$ (Figure 2). The $70 \mu\text{m}$ flux possibly contains the emission from the central star, and this temperature gives an upper limit of the dust temperature. Using these values, the mass of the dust condensation associated with B59#11 is estimated to be $0.09 \pm 5.3 \times 10^{-4} M_\odot$. The FWHM of the 1.1 mm dust condensation associated with B59#11 is $37'' \times 33''$ (PA= -47°), and the deconvolved size cannot be estimated, since the dust condensation is not resolved. Román-Zúñiga et al. (2012) estimated that the deconvolved size of the dust condensation associated with B59#11 is $18'' \times 17''$ from the 1.2 mm dust-continuum observations with a beam size of $11''$. Using this value, the mean gas density, n , is estimated by assuming a spherically symmetric shape and using a geometric mean radius, as follows;

$$n = \frac{M_{\text{dust}}}{(4/3)\pi[\sqrt{(D_{\text{maj}}/2)(D_{\text{min}}/2)}]^3 \mu_g m_{\text{H}_2}} \quad (2)$$

D_{maj} and D_{min} are source sizes along major and minor axes, respectively. μ_g is mean atomic weight set to 1.36. The mean gas density is estimated to be $n = 1.9 \times 10^6 \text{ cm}^{-3}$.

3.1.2. *ASTE $^{12}\text{CO}(3-2)$ Emission*

Our ASTE CO(3–2) data show that the CO(3–2) line profiles around B59#11 have high velocity wings that probably originate from the molecular outflow ejected from B59#11 (Figure 5). Here, we identify a molecular outflow from B59#11 using the ASTE CO(3–2) data, and derive the physical properties of the outflow (Table 4).

From the inspection of the CO(3–2) velocity channel maps (Figure 3) and the profile map (Figure 5), we consider that the cloud component has a velocity range of $V_{\text{LSR}} = 1.5 - 5.5 \text{ km s}^{-1}$. The components with velocities smaller than $V_{\text{LSR}} = 1.5 \text{ km s}^{-1}$ and larger than 5.5 km s^{-1} are considered to correspond to the blueshifted and redshifted molecular outflow components, respectively. The main characteristics of the CO(3–2) data are summarized as follows;

- a) Both the blueshifted and redshifted emissions are seen on the northeast of B59#11 with lengths of $\sim 0.2 \text{ pc}$ and $\sim 0.1 \text{ pc}$, respectively.
- b) High velocity emission is mostly centered on B59#11.
- c) The CO(3–2) profiles have high-velocity wings that probably originate from the outflows from the YSOs, [BHB2007]#1, #9, and #10. The outflow lobes of these YSOs can be recognized in Figure 3.

The high velocity wings associated with B59#11 noted above a) are roughly aligned in the same direction as the extended nebulosity seen in IRAC $3.6 \mu\text{m}$ and $4.5 \mu\text{m}$ images (Brooke et al. 2007), indicating that these high velocity components are the outflow wings. The cavity-like structure on the northeast of B59#11 seen in the AzTEC/ASTE 1.1 mm dust-continuum image coincides with the outflow; especially redshifted emission on the northeast of B59#11 is possibly well fit to the cavity. The characteristics, a) and b) above,

indicate that the outflow associated with B59#11 is nearly along the plane of the sky direction and dominates the high velocity emission in the B59 region. These overall features are in good agreement with the CO(3–2) maps in Duarte-Cabral et al. (2012).

Figure 5 (b) shows a profile map of the $80'' \times 80''$ area around B59#11 with a grid spacing of $20''$. Strong redshifted wing (and weaker blueshifted emission) exists on the southwest of B59#11, while both the blueshifted and redshifted emissions are seen on the northeast.

We derived physical properties of the outflow using an excitation temperature of 25 K and an outflow inclination angle of 75° following Duarte-Cabral et al. (2012). We assumed the local thermal equilibrium (LTE) condition and used the following equation;

$$M_j = \mu_g m_{\text{H}_2} X_{\text{CO}}^{-1} \Omega d^2 \sum_i N_{\text{CO},i,j} \quad (3)$$

$$= 4.65 \times 10^{-7} \left(\frac{X_{\text{CO}}}{1.0 \times 10^{-4}} \right)^{-1} \left(\frac{d}{130 \text{pc}} \right)^2 \left(\frac{\theta}{22''} \right)^2 \left(\frac{\eta}{0.5} \right)^{-1} \sum_i \left(\frac{T_{\text{A},i,j}^*}{\text{K} \cdot \text{km s}^{-1}} \right) \left(\frac{T_{\text{ex}}}{25 \text{K}} \right) \exp [33.2/T_{\text{ex}}] M_\odot \quad (4)$$

The mass, momentum, and kinetic energy of the outflow are summarized in Table. 4.

3.2. The Dense Gas Distribution in B59#11

3.2.1. ASTE HCO^+ and H^{13}CO^+ (4–3) observations

Here, we present the dense gas distribution associated with B59#11. Figure 6 shows a 5×5 points profile map in ASTE HCO^+ (4–3) emission (black lines) taken toward B59#11 with a grid spacing of $20''$, together with a 3×3 points profile map in H^{13}CO^+ (4–3) emission (red lines) with the same grid spacing. The HCO^+ (4–3) emission extends over the $80'' \times 80''$ area. The strongest emission exists on the southwest of B59#11, $(-40, -20)$, and has a peak

temperature of $\sim 2.5 \pm 0.12$ K (T_A^*). The dotted line in Figure 7 (b) shows the residual spectrum after subtracting an average of the surrounding four spectra from that at the center. A high velocity component ($V_{\text{LSR}} = -1.5$ – 2.5 km s $^{-1}$, 5.0 – 8.0 km s $^{-1}$) exists in both the central and residual spectra. After comparing both spectra, we found that the high velocity component is mostly spatially unresolved with the ASTE $22''$ beam (corresponding to ~ 3000 AU). The velocity width of the high velocity component in HCO $^+$ emission is almost the same as that of the dense gas rotation, $V_{\text{LSR}} = -0.5$ – 8.2 km s $^{-1}$ in SMA ^{13}CO ($V_{\text{LSR}} = 0.0$ – 7.7 km s $^{-1}$) emission (see Section 3.2.2), and it implies that the high velocity component corresponds to the rotating dense gas.

The velocity shift of 0.42 km s $^{-1}$ is detected along the direction from the northwest ($20''$, $-20''$) to the southeast ($-20''$, $20''$) of B59#11 in the HCO $^+$ line (Figure 7), and this direction coincides with that of the velocity shift associated with dense gas rotation as inferred from the SMA ^{13}CO and C ^{18}O emissions (Section 3.2.2). This means that the velocity shift in HCO $^+$ emission possibly arises from the large-scale envelope rotation. The specific angular momentum of the outer envelope is estimated to be 3.7×10^{-3} km s $^{-1}$ pc if the shift is due to the rotation.

The H $^{13}\text{CO}^+(4-3)$ intensity is strongest at the center ($T_A^* \sim 0.11$ K) and no clear signature of self-absorption is found. The peak velocity and the FWHM velocity width of the central spectrum are obtained to be 3.6 km s $^{-1}$ and as wide as 1.7 km s $^{-1}$. The peak velocity of 3.6 km s $^{-1}$ is adopted as the systemic velocity of B59#11 in this paper. The H $^{13}\text{CO}^+(4-3)$ spectra are very narrow at other positions; e.g., positions at ($0''$, $20''$) and ($20''$, $-20''$).

From the comparison of the HCO $^+$ and H $^{13}\text{CO}^+$ line profiles, the emissions in H $^{13}\text{CO}^+$ correspond to the dips in HCO $^+$ in velocity; a dip is located at 3 – 4 km s $^{-1}$ and emission is located at 2 – 5 km s $^{-1}$ at the center. It indicates that the dips are formed by self-absorption.

On the other hand, the HCO^+ intensities at the blueshifted parts are stronger than the redshifted parts on the southwest of B59#11, for example, $(-20'', 0'')$ and $(-20'', -20'')$ in Figure 6. These "blue-skewed" profiles are usually considered to indicate dynamical infall (e.g., Zhou et al. 1993). It is noted that a red-skewed profile is obtained at the central part of B59#11, and a simple infall model cannot account for the overall observational results.

Masses of the high velocity components in HCO^+ emission are estimated using the following equation on the assumption of LTE condition.

$$\begin{aligned}
 M_{\text{HCO}^+} &= \mu_g m_{\text{H}_2} X_{\text{HCO}^+}^{-1} \Omega d^2 \int N_{\text{HCO}^+} dv & (5) \\
 &= 1.03 \times 10^{-2} \left(\frac{X_{\text{HCO}^+}}{1.0 \times 10^{-10}} \right)^{-1} \left(\frac{d}{130 \text{pc}} \right)^2 \left(\frac{\theta}{22''} \right)^2 \left(\frac{\eta}{0.5} \right)^{-1} \\
 &\quad \int \left(\frac{T_A^*}{\text{K} \cdot \text{km s}^{-1}} \right) dv \left(\frac{T_{\text{ex}}}{30 \text{K}} \right) \exp [42.8/T_{\text{ex}}] M_{\odot} & (6)
 \end{aligned}$$

where we assume that HCO^+ emission is optically thin in the high velocity ranges. We used $X[\text{HCO}^+] = 1.0 \times 10^{-10}$ (Rawlings et al. 2004), and $T_{\text{ex}} = 30 \text{ K}$, which we adopt for the envelope/disk in this paper (Section 3.1.1) since its high velocity component is considered to trace the rotating dense gas. The masses of the blueshifted ($V_{\text{LSR}} = -1.5 - 2 \text{ km s}^{-1}$) and redshifted ($V_{\text{LSR}} = 5 - 8 \text{ km s}^{-1}$) components are estimated to be 1.2×10^{-2} and $1.8 \times 10^{-2} M_{\odot}$, respectively. The total mass of the high velocity components, $0.03 M_{\odot}$, is comparable to the masses obtained from SMA ^{13}CO and C^{18}O data. This indicates that the high velocity components trace the dense gas rotation in terms of the mass comparison as well as the comparison of the velocity width described above.

The mass of dense region traced by $\text{H}^{13}\text{CO}^+(4-3)$ is estimated on the assumption of LTE condition.

$$\begin{aligned}
 M_{\text{H}^{13}\text{CO}^+} &= \mu_g m_{\text{H}_2} X_{\text{H}^{13}\text{CO}^+}^{-1} \Omega d^2 \int N_{\text{H}^{13}\text{CO}^+} dv & (7) \\
 &= 7.8 \times 10^{-1} \left(\frac{X_{\text{H}^{13}\text{CO}^+}}{1.4 \times 10^{-12}} \right)^{-1} \left(\frac{d}{130 \text{pc}} \right)^2 \left(\frac{\theta}{22''} \right)^2 \left(\frac{\eta}{0.5} \right)^{-1}
 \end{aligned}$$

$$\int \left(\frac{T_A^*}{\text{K} \cdot \text{km s}^{-1}} \right) dv \left(\frac{T_{\text{ex}}}{30\text{K}} \right) \exp [41.6/T_{\text{ex}}] M_{\odot} \quad (8)$$

We adopt $X[\text{H}^{13}\text{CO}^+] = 1.4 \times 10^{-12}$ estimated with a C to ^{13}C abundance ratio of ~ 71 (Wilson & Rood 1994). H^{13}CO^+ emission is assumed to be optically thin, and we obtained a mass of $0.59 M_{\odot}$. These results are summarized in Table. 5.

3.2.2. SMA $^{13}\text{CO}(2-1)$ and $\text{C}^{18}\text{O}(2-1)$ Emission

In this section, we show the results of SMA ^{13}CO and $\text{C}^{18}\text{O}(2-1)$ observations. These emissions are expected to trace the smaller scale of the dense gas than that obtained by ASTE HCO^+ and H^{13}CO^+ observations. From the total integrated intensity maps (Figure 8 (c) and (d)), it is shown that a compact gas condensation in ^{13}CO and C^{18}O emissions is clearly associated with B59#11 and elongated along northwest-southeast direction, which is perpendicular to the molecular outflow axis identified with ASTE $\text{CO}(3-2)$ observations (Section 3.1.2). The size of the C^{18}O condensation is about half the size of the ^{13}CO condensation, and its extent are measured to be $17'' \times 11''$ (corresponding to $\sim 2000 \times 1400$ AU and an aspect ratio of ~ 1.5) and $30'' \times 17''$ (corresponding to $\sim 4000 \times 2000$ AU and an aspect ratio of ~ 1.8), respectively.

A velocity gradient is evident in both the ^{13}CO and the C^{18}O maps (Figure 8) along the major axis of the dense gas condensation. The northwestern side of the condensation is blueshifted and the southeastern side is redshifted. Figure 11 (a) and (b) show the Position-Velocity (P-V) diagrams which are cut along the major axis of the condensation. The velocity gradient appears to have a power-law profile, indicating that the velocity gradient is arisen from the dense gas rotation. The specific angular momentum is estimated to be $2.1 \pm 1.2 \times 10^{-3} \text{ km s}^{-1} \text{ pc}$ using the results of $^{13}\text{CO}(2-1)$ assuming the inclination angle of 75° (Duarte-Cabral et al. 2012).

The optical depth of $^{13}\text{CO}(2-1)$ emission is calculated assuming that the abundance ratio between ^{13}CO and C^{18}O is ~ 6 (Frerking et al. 1987) and use the following equation,

$$\frac{T_{\text{R}}^*(^{13}\text{CO})_v}{T_{\text{R}}^*(\text{C}^{18}\text{O})_v} = \frac{1 - \exp[-\tau_v(^{13}\text{CO})]}{1 - \exp[-\tau_v(^{13}\text{CO})/6]} \quad (9)$$

where T_{R}^* is the radiation temperature at a given velocity, v . The ^{13}CO emission is estimated to be optically thick for only two velocity channels that are closed to the systemic velocity, $V_{\text{LSR}} = 3.3 - 4.4 \text{ km s}^{-1}$. Noted that emissions in the channels severely suffer from resolved-out effect in both lines, and thus our estimate of the optical depth includes a large uncertainty due to such effect. On the assumption of LTE condition, we also obtain the mass of dense gas traced by $^{13}\text{CO}(2-1)$ emission as follows;

$$M_{^{13}\text{CO}} = \sum_j M_j = 5.11 \times 10^{-5} \left(\frac{X_{^{13}\text{CO}}}{1.7 \times 10^{-6}} \right)^{-1} \left(\frac{d}{130\text{pc}} \right)^2 \sum_i \left(\frac{S_{\nu,i,j}}{\text{Jy} \cdot \text{km s}^{-1}} \right) \left(\frac{T_{\text{ex}}}{30\text{K}} \right) \exp[15.9/T_{\text{ex}}] \frac{\tau_{^{13}\text{CO}}}{1 - e^{-\tau_{^{13}\text{CO}}}} M_{\odot} \quad (10)$$

We used $T_{\text{ex}} = 30 \text{ K}$ and $X[^{13}\text{CO}] = 1.7 \times 10^{-6}$ (Frerking et al. 1987). From a total integrated flux of $30.4 \text{ Jy} \cdot \text{km s}^{-1}$, the mass is estimated to be $3.7 \times 10^{-2} M_{\odot}$. On the assumption of LTE condition and optically thin emission (Frerking et al. 1982), we compute the mass of dense gas traced by $\text{C}^{18}\text{O}(2-1)$ emission as follows;

$$M_{\text{C}^{18}\text{O}} = \sum_j M_j = 3.03 \times 10^{-4} \left(\frac{X_{\text{C}^{18}\text{O}}}{3.0 \times 10^{-7}} \right)^{-1} \left(\frac{d}{130\text{pc}} \right)^2 \sum_i \left(\frac{S_{\nu,i,j}}{\text{Jy} \cdot \text{km s}^{-1}} \right) \left(\frac{T_{\text{ex}}}{30\text{K}} \right) \exp[15.6/T_{\text{ex}}] M_{\odot} \quad (11)$$

We adopt $T_{\text{ex}}=30 \text{ K}$ and $X[\text{C}^{18}\text{O}] = 3.0 \times 10^{-7}$ (Frerking et al. 1987). Using a total integrated flux of $8.9 \text{ Jy} \cdot \text{km s}^{-1}$, the mass is derived to be $3.3 \times 10^{-2} M_{\odot}$.

3.3. SMA 1.3 mm Dust-Continuum Emission

Figure 9 shows the distribution of 1.3 mm dust-continuum emission obtained by SMA. A compact and strong dust condensation associated with B59#11, centered at $(\alpha_{J2000.0}, \delta_{J2000.0}) = (17^{\text{h}}11^{\text{m}}23^{\text{s}}.08, -27^{\circ}24'33''.1)$, has been detected. The FWHM size of the dust condensation is measured to be $5''.5 \times 3''.5$ (PA=22°), and its deconvolved size is estimated to be $2''.7 \times 1''.4$ ($\sim 350 \times 180$ AU) (PA=-15°). The condensation is oriented along the same direction with the elongation of the dense gas distributions in SMA ^{13}CO and C^{18}O emissions (see Section 3.6 and Section 4.1). The peak intensity and total integrated flux density are 0.49 ± 0.012 Jy beam $^{-1}$ and 0.67 Jy, respectively. The mass and mean gas density are estimated to be $\sim 7.3 \times 10^{-2} M_{\odot}$ and 1.1×10^9 cm $^{-3}$, using Equation (1) on the same assumptions as those in the estimate for the AzTEC/ASTE 1.1 mm data (see Section 3.1). The separation between the position of B59#11 defined by Forbrich et al. (2009) and the SMA peak position is $\sim 0''.3$, i.e. smaller than the position accuracy of the infrared images. At the position of B59#11SW, no dust condensation has been detected and the disk or envelope mass associated with B59#11SW is estimated to be lower than $4.9 \times 10^{-4} M_{\odot}$ (3σ noise level) with $\beta = 2$. This suggests that B59#11SW is not embedded in the massive envelope and may be considered to be a more evolved source.

3.4. SMA $^{12}\text{CO}(2-1)$ Emission

— The velocity Gradient in the Molecular Outflow —

We have detected an interesting internal structure in the outflow associated with B59#11 as shown below.

Figure 10 shows blueshifted ($V_{\text{LSR}} = -4.9$ - 1.4 km s $^{-1}$) and redshifted ($V_{\text{LSR}} = 4.6$ - 12 km s $^{-1}$) components detected by SMA $\text{CO}(2-1)$ observations. We identified three blueshifted

and redshifted lobes in Figure 10; one blueshifted and one redshifted lobes are projected towards the northeastern side of B59#11, while the third, redshifted lobe is projected toward the southwestern side. The lengths of the lobes are ~ 2400 AU, 3100 AU, and 2400 AU, respectively. In both maps of ASTE CO(3–2) and SMA CO(2–1), the blueshifted and redshifted components exist on the northeastern side of B59#11, while only a redshifted component exists on the southwestern side. This shows that the high velocity components observed in the SMA CO map trace the molecular outflow ejected from B59#11. The mean velocity map of SMA CO emission (Figure 10 (b)) shows the velocity gradient in the outflow lobe located on the northeast; the northern side of the outflow lobe is blueshifted and the southern side is redshifted. The direction of the velocity gradient in the outflow is the same as that of the dense gas rotation shown in Section 3.2.2.

The mass, momentum, and energy are estimated from the following equation;

$$M_{12\text{CO}} = \sum_j M_j = 6.09 \times 10^{-7} \left(\frac{X_{12\text{CO}}}{1.0 \times 10^{-4}} \right)^{-1} \left(\frac{d}{130\text{pc}} \right)^2 \sum_i \left(\frac{S_{\nu,i,j}}{\text{Jy} \cdot \text{km s}^{-1}} \right) \left(\frac{T_{\text{ex}}}{25\text{K}} \right) \exp[16.6/T_{\text{ex}}] M_{\odot} \quad (12)$$

We apply the same parameters as those of Equation 4 in Section 3.1.2 and assume that CO(2–1) emission is optically thin. The masses for the blueshifted and redshifted outflows are derived to be 2.8×10^{-4} and $4.4 \times 10^{-4} M_{\odot}$, respectively. It is noted that CO lines often become optically thick even toward outflow wing components, and thus, the estimates of the outflow mass, momentum, or energy are probably lower limits. Moreover, it is shown that roughly 90 % of the emission is resolved-out in SMA data, by comparison with the flux density estimated from ASTE CO(3–2) emission. The energies and momentums are also summarized in Table. 4 together with the masses.

4. Discussion

4.1. Kinematics and physical properties of the rotating envelope and disk

4.1.1. Kinematical evidence for the formation of the Keplerian disk

As described in Section 3.2.2, ^{13}CO and $\text{C}^{18}\text{O}(2-1)$ emissions are oriented perpendicular to the outflow direction and also show the velocity gradient along its major axis, probably tracing a rotating flattened envelope or a disk of dense gas. The specific angular momentum of this system is as large as $2.1 \times 10^{-3} \text{ km s}^{-1} \text{ pc}$ (as described in Section 3.2.2). It is, therefore, expected that the centrifugal radius ($= j_n^2/GM_*$), which is the radius at the outer edge of the rotationally supported disk, is also as large as 200-1000 AU for e.g., $M_* = 0.2 - 1 M_\odot$ and such a Keplerian disk can be identified. Here, we discuss whether the velocity gradient traces the rotation of the Keplerian disk or not in terms of the radial dependence of the rotation velocity.

Investigating the radial dependences of the rotational velocities allows us to discriminate two possible kinematics; the velocities should be proportional to r^{-1} and $r^{-1/2}$ for a rotation conserving its angular momentum and a Keplerian rotation, respectively. We plotted radii as a function of velocities in ^{13}CO and C^{18}O emissions as shown in Figure 12. The radii are estimated by measuring the peak positions of emissions and deriving the separations from the 1.3 mm dust-continuum peak. Via χ^2 minimizations, the power-law indexes, α (i.e., $v = r^\alpha + v_{\text{sys}}$) in ^{13}CO and C^{18}O emissions are estimated to be -1.3 and -0.61, respectively (details are shown in Table 6). These results suggest that the outer and lower density regions traced by the ^{13}CO are in better agreement with the presence of a rotating-flattened envelope, while the inner, more dense regions traced by C^{18}O emission (or, at least, some parts of this region) are in better agreement with the presence of a rotationally supported disk.

The existence of a disk traced by C¹⁸O can be also inferred from comparison between a dynamical mass and a stellar mass obtained from the SED analysis. To derive the dynamical mass of B59#11, we fit Keplerian rotation (i.e., $v(r) = \sin i \sqrt{\frac{GM_*}{r}}$) to the C¹⁸O data (Figure 12). The central stellar mass is estimated to be $0.73^{+0.53}_{-0.39} M_\odot$ assuming the inclination angle, i , of 75° . This is an upper limit to the central mass value, since this inclination angle is determined by the limitation of the outflow opening angle which gives a lower limit. The central stellar mass estimated from this fitting is not consistent with the $0.28 M_\odot$ obtained from the SED model fitting conducted by Riaz et al. (2009) using the radiative transfer model of Whitney et al. (2003) for $i=53^\circ$ - 59° . Our observations, however, reveal that the outflow associated with B59#11 is ejected mostly in the plane of the sky (Section 3.1.2). We also run the SED model fitting program developed by Robitaille et al. (2007) assuming $i > 75^\circ$, and obtained the central stellar mass of $0.81 M_\odot$ as the best fit result. This model gives a better fit to data at the shorter wavelengths, $\lambda < 70 \mu\text{m}$, where emission comes mostly from the central protostar or the central region, compared with the model of Riaz et al. (2009) (Figure 2). The fit is, however, worse at the longer wavelengths, especially at $70 \mu\text{m}$ and this might be caused by the contamination of B59#11SW due to the larger observing beams ($8''$ - $36''$). The estimated stellar mass from this SED analysis is well agreed with the dynamical mass obtained from SMA C¹⁸O data, and this suggests a rotationally supported Keplerian disk traced by C¹⁸O emission.

4.1.2. Evidence for disk formation from 1.3 mm image

Next, we also discuss whether the SMA 1.3 mm dust-continuum emission traces the disk/envelope system or exclusively the envelope. Here, we follow Jørgensen et al. (2009). They have pointed out that the SMA flux density (in 1.1 mm continuum emission) is only several % of that of single dish observations (in $850 \mu\text{m}$ continuum emission) if there is

no disk contribution about a protostar located at a distance of 125 pc. Here, we convert the distance and wavelengths in our observations to match with their method. Using the SMA data with the baselines $\geq 52 \text{ k}\lambda$, the SMA to AzTEC flux density ratio is estimated to be $16 \pm 2\%$ where the flux densities are converted using $\beta = 1$ (Section 3.1.1). This value is large enough to be compared with 8%, which is the largest value of the envelope contribution toward the various envelope models, suggesting the existence of the disk. We also note that the deconvolved size of the 1.3 mm dust condensation, $2.8'' (\sim 350 \text{ AU})$, is consistent with an expected disk size of approximately 300 AU, which is obtained from the estimation of the centrifugal radius using the central stellar mass of $0.73 M_{\odot}$ (Section 4.1.1). The position angle is also consistent with the direction of the velocity gradient, would be another sign that the 1.3 mm dust-continuum emission traces the disk.

The SMA emission could be separated to contributions from the disk and the envelope, and individual masses are estimated using the following equations (Jørgensen et al. 2009).

$$S_{50\text{k}\lambda} = S_{\text{disk}} + c \cdot S_{\text{env}} \quad (13)$$

$$S_{15''} = S_{\text{disk}} + S_{\text{env}} \quad (14)$$

c is a fraction of an envelope contribution to emission obtained by interferometric observations. On the assumption of $c=0.04$ (Jørgensen et al. 2009) and the same parameters as those in Section 3.1.1 and Section 3.3, the envelope and disk masses are estimated to be 8.2×10^{-2} and $1.5 \times 10^{-2} M_{\odot}$, respectively.

From the above discussion, we conclude that, in source B59#11, a rotationally supported disk has formed and it is in an early evolutionary phase.

4.2. Comparison of physical natures in Keplerian disks between B59#11 and L1551NE

Recently, a Keplerian disk was found in the proto-binary system L1551NE, which is a young Class-I protostar with a low bolometric temperature (T_{bol}) of 91 K (Takakuwa et al. 2012). B59#11 also has a low bolometric temperature of 70 K, comparable to that of L1551NE. Thus, the comparison with L1551NE provides us with valuable information of a disk formation in the early phases of protostellar evolution.

The dust mass associated with L1551NE obtained from the SMA observations is $0.016 M_{\odot}$ (Takakuwa et al. 2012). This compares well to that obtained for B59#11 of $0.015 M_{\odot}$ (see Section 4.1.2) using the same mass opacity coefficient. The disk mass, central stellar mass, and the bolometric temperature of B59#11 are comparable with those of L1551NE as shown in Table 8. The disk sizes are possibly similar, too. On the other hand, the disk around B59#11 is a proto”stellar” disk, while the disk in L1551NE is a proto”binary” disk.

Machida et al. (2004) have revealed that a disk is hard to fragment under a strong magnetic field even if the initial specific angular momentum is large. On the other hand, Román-Zúñiga et al. (2012) have suggested that a magnetic field with a strength of $\sim 0.1\text{-}0.2$ mG is required to support the B59 clump against further fragmentation. This value seems to be larger than the strength of the magnetic field in the Taurus molecular cloud ($\sim 10\text{-}50$ μG ; Levin et al. 2001; Crutcher et al. 2003). Thus, the strong magnetic field may keep B59#11 being a single protostar.

Recent theoretical studies suggest that extended Keplerian disks may not be formed in the early phase of protostellar evolution, i.e., Class-0 phase (e.g., Hennebelle & Fromang 2008; Dapp et al. 2012; Krasnopolsky et al. 2012). However, previous observations have shown that large Keplerian disks exist in the Class-I phase. In this paper, we have revealed that the Class-0/I protostar, B59#11 has a large Keplerian disk with a size of 350 AU.

Very recently, Tobin et al. (2012) also discovered a large Keplerian disk around the Class-0 object, L1527. Hence, it remains unclear in what stage large Keplerian disks are formed. Further observational and theoretical studies are required to constraining the formation process of Keplerian disks in the protostellar evolution.

4.3. A rotating outflow in B59#11?

It is shown that there is a velocity gradient along the same direction as that of the envelope rotation in the B59#11 outflow (Section 3.4). There are some interpretations of this velocity gradient, and one of these is a rotating outflow. The rotations of the outflows in CO observations were reported in the Class-I and II sources (e.g., Launhardt et al. (2009); Pech et al. (2012)). The velocity structure in the northeastern lobe of the B59#11 outflow is very similar to those in outflows ejected from the Class-II YSO, CB26 (Launhardt et al. 2009), and the Class-I YSO, HH797 (Pech et al. 2012), which are two very reliable candidates for a rotating molecular outflow. The specific angular momentum of the outflow in B59#11 is estimated to be $\sim 2.3 \times 10^{-3} \text{ km s}^{-1} \text{ pc}$ from a separation of the peak positions of blueshifted and redshifted lobes of $\sim 4''$ (corresponding to 520 AU), a radial velocity of 1.8 km s^{-1} (Figure 10 and 11), and the inclination angle of 75° . It is noted that this value is almost the same as that of CB26 and smaller than that of HH797.

Another possibility is the outflow ejected from a protobinary system. Such a molecular outflow is identified in, for example, IRAS 05295+1247 (Arce & Sargent 2005), whose outflow is composed of one blueshifted lobe and three redshifted lobes and may show a resemblance to the B59#11 outflow. An outflow from a protobinary system, however, often shows a X-shaped structure, which comprises the walls of a cone-shaped outflow cavity, or the S-shaped structure, which is formed by a precessing outflow (e.g., Arce & Sargent (2005); Wu et al. (2009)). These structures are not confirmed in B59#11 (Figure 10).

B59#11 might constitute a binary system with the nearby (projected separation is 1000 AU) protostar, B59#11SW, as suggested by Riaz et al. (2009). Assuming that the precession of the outflow axis is driven by tidal interactions between the circumstellar disk from which the jet is launched and a companion star on a non-coplanar orbit (e.g. Launhardt et al. 2009), the precessing timescale is expected to be the same as the binary orbital period. If the stellar masses of B59#11 and B59#11SW are both close to $1 M_{\odot}$, the orbital period is estimated to be $\sim 10^5$ yr assuming that the binary separation is 4000 AU ($\sim 1000 \text{ AU} / \cos i$, $i = 75^\circ$) from the equation, $T^2 = \frac{4\pi^2}{G(M_1+M_2)}a^3$ ¹. This period would be much longer than the outflow dynamical timescale of $\sim 10^4$ yr (Duarte-Cabral et al. 2012) obtained from their single-dish observations. Thus, the kinematics of the B59#11 outflow can not be explained by the precession caused by such a very wide binary.

Is there really no evidence that B59#11 is a closed binary system? If a binary system is formed, the tidal effects of the two protostars can transport rotational angular momentum of the common disk outwards and create a hole with a radius of $\sim 2.7 \times$ (semi major axis of the binary orbital) (e.g., Artymowicz et al. (1991); Dutrey et al. (1994)). Such signature sometimes appears in, e.g., C¹⁸O and/or ¹³CO images and P-V diagrams; continuous increasing of the rotation velocity as $r^{-1/2}$ and r^{-1} is terminated at the inner edge of the disk. As discussed in Section 4.1.1, the dense inner part traced by C¹⁸O is likely to be a rotationally supported disk. And the high velocity emission in ¹³CO perhaps also traces the disk as shown in Figures 11 and 12. The highest velocity of the envelope/disk rotation is about 4.6 km s^{-1} in ¹³CO, and the rotation velocity is estimated to trace $r=30$ AU region if we assume that ¹³CO emission traces the Keplerian disk at the inner area. The binary separation is calculated to be smaller than $11(=30/2.7)$ AU if we assume that the obtained

¹ T , $M_1 + M_2$, and a is a binary orbital period, masses of a primary and the secondary, and a semi major axis of the binary orbital, respectively.

radius is an upper limit to that of the inner edge of the disk and a binary companion exists. Further observations with higher spatial resolution are needed to confirm the outflow rotation in B59#11.

5. Conclusions

We have carried out the ASTE observations toward the B59 region ($d \sim 130$ pc) and a Class-0/I YSO, B59#11 in the Pipe Nebula in 1.1 mm dust-continuum, CO(3–2), HCO⁺, and H¹³CO⁺(4–3) emissions. We also processed archival data from the SMA observations of B59#11 in 1.3 mm dust-continuum, CO, ¹³CO, and C¹⁸O(2–1) emissions. The main results of these data are summarized as follows;

1. We have detected four dust condensations associated with YSOs, [BHB2007]#1, #9, #10, and #11 with the AzTEC/ASTE 1.1 mm continuum observations. The dust-continuum emission associated with B59#11 is the strongest in the B59 region, and the mass of the condensation is estimated to be $0.09 M_{\odot}$.
2. From ASTE CO(3–2) observations, we found that B59#11 is blowing a collimated outflow whose axis is almost on the plane of the sky. This outflow traces well a cavity-like structure seen in the AzTEC/ASTE 1.1 mm dust-continuum map. The overall structures are in good agreement with the results by Duarte-Cabral et al. (2012).
3. The images of SMA ¹³CO and C¹⁸O(2–1) emissions with a resolution of $\sim 5''$ (corresponding to ~ 650 AU) have revealed that a compact and elongated structure of the dense gas is associated with B59#11 with a size of about 4000×2000 AU (with an aspect ratio of $\sim 2:1$). The dense gas shows a rotation along its major axis and the specific angular momentum is estimated to be $2.1 \times 10^{-3} \text{ km s}^{-1} \text{ pc}$. ASTE HCO⁺

emission also shows a velocity gradient, which is considered to be arisen from the large-scale envelope rotation.

4. A compact dust-continuum condensation with a mass of $7.3 \times 10^{-2} M_{\odot}$ is identified from our SMA data in 1.3 mm continuum emission. The deconvolved size of the dust condensation is estimated to be $\sim 350 \times 180$ AU, and is oriented along the rotation axis of the dense gas.
5. The SMA CO(2–1) emission map shows a velocity gradient in the outflow lobe. It is considered to trace the outflow rotation and its specific angular momentum is estimated to be $2.3 \times 10^{-3} \text{ km s}^{-1} \text{ pc}$. This specific angular momentum is comparable to that of another rotating outflow, CB26. Further observations with higher spatial resolution, however, are needed to confirm the rotation of the B59#11 outflow.
6. The radial velocities in SMA ^{13}CO and $\text{C}^{18}\text{O}(2-1)$ emissions have different power-law indexes, and estimated to be -1.3 and -0.61, respectively, implying that C^{18}O emission traces a Keplerian disk. The existence of the disk is also suggested from our analysis of ASTE and SMA data in dust-continuum emissions. The disk mass and the central stellar mass are estimated to be 0.03 and $0.73 M_{\odot}$, respectively.

REFERENCES

- Alves, F. O., & Franco, G. A. P. 2007, *A&A*, 470, 597
- Arce, H. G., & Sargent, A. I. 2005, *ApJ*, 624, 232
- Artymowicz, P., Clarke, C. J., Lubow, S. H., & Pringle, J. E. 1991, *ApJ*, 370, L35
- Beckwith, S. V. W., & Sargent, A. I. 1991, *ApJ*, 381, 250
- Brinch, C., Crapsi, A., Jørgensen, J. K., Hogerheijde, M. R., & Hill, T. 2007, *A&A*, 475, 915
- Brooke, T. Y., Huard, T. L., Bourke, T. L., et al. 2007, *ApJ*, 655, 364
- Covey, K. R., Lada, C. J., Román-Zúñiga, C., et al. 2010, *ApJ*, 722, 971
- Crutcher, R., Heiles, C., & Troland, T. 2003, in *Lecture Notes in Physics*, Berlin Springer Verlag, Vol. 614, *Turbulence and Magnetic Fields in Astrophysics*, ed. E. Falgarone & T. Passot, 155–181
- Dapp, W. B., Basu, S., & Kunz, M. W. 2012, *A&A*, 541, A35
- Duarte-Cabral, A., Chrysostomou, A., Peretto, N., et al. 2012, *A&A*, 543, A140
- Dutrey, A., Guilloteau, S., & Simon, M. 1994, *A&A*, 286, 149
- Emerson, D. T., & Graeve, R. 1988, *A&A*, 190, 353
- Ezawa, H., Kawabe, R., Kohno, K., & Yamamoto, S. 2004, in *Society of Photo-Optical Instrumentation Engineers (SPIE) Conference Series*, Vol. 5489, *Society of Photo-Optical Instrumentation Engineers (SPIE) Conference Series*, ed. J. M. Oschmann, Jr., 763–772
- Forbrich, J., Lada, C. J., Muench, A. A., Alves, J., & Lombardi, M. 2009, *ApJ*, 704, 292

Frerking, M. A., Langer, W. D., & Wilson, R. W. 1982, *ApJ*, 262, 590

—. 1987, *ApJ*, 313, 320

Hennebelle, P., & Fromang, S. 2008, *A&A*, 477, 9

Hildebrand, R. H. 1983, *QJRAS*, 24, 267

Jørgensen, J. K., van Dishoeck, E. F., Visser, R., et al. 2009, *A&A*, 507, 861

Kawabe, R., Tsukagoshi, T., & Shimajiri, Y. 2013, in preparation

Knacke, R. F., & Thomson, R. K. 1973, *PASP*, 85, 341

Kohno, K., Yamamoto, S., Kawabe, R., et al. 2004, in *The Dense Interstellar Medium in Galaxies*, ed. S. Palfzner, C. Kramer, C. Staubmeier, & A. Heithausen, 349

Krasnopolsky, R., Li, Z.-Y., Shang, H., & Zhao, B. 2012, *ApJ*, 757, 77

Kutner, M. L., & Ulich, B. L. 1981, *ApJ*, 250, 341

Launhardt, R., Pavlyuchenkov, Y., Gueth, F., et al. 2009, *A&A*, 494, 147

Lee, C.-F. 2010, *ApJ*, 725, 712

Levin, S. M., Langer, W. D., Velusamy, T., Kuiper, T. B. H., & Crutcher, R. M. 2001, *ApJ*, 555, 850

Liu, G., Calzetti, D., Yun, M. S., et al. 2010, *AJ*, 139, 1190

Lombardi, M., Alves, J., & Lada, C. J. 2006, *A&A*, 454, 781

Lommen, D., Jørgensen, J. K., van Dishoeck, E. F., & Crapsi, A. 2008, *A&A*, 481, 141

Machida, M. N., Tomisaka, K., & Matsumoto, T. 2004, *MNRAS*, 348, L1

- Motte, F., & André, P. 2001, *A&A*, 365, 440
- Onishi, T., Kawamura, A., Abe, R., et al. 1999, *PASJ*, 51, 871
- Pech, G., Zapata, L. A., Loinard, L., & Rodríguez, L. F. 2012, *ApJ*, 751, 78
- Rathborne, J. M., Lada, C. J., Muench, A. A., Alves, J. F., & Lombardi, M. 2008, *ApJS*, 174, 396
- Rawlings, J. M. C., Redman, M. P., Keto, E., & Williams, D. A. 2004, *MNRAS*, 351, 1054
- Riaz, B., Martín, E. L., Bouy, H., & Tata, R. 2009, *ApJ*, 700, 1541
- Robitaille, T. P., Whitney, B. A., Indebetouw, R., & Wood, K. 2007, *ApJS*, 169, 328
- Román-Zúñiga, C. G., Frau, P., Girart, J. M., & Alves, J. F. 2012, *The Astrophysical Journal*, 747, 149
- Román-Zúñiga, C. G., Lada, C. J., & Alves, J. F. 2009, *The Astrophysical Journal*, 704, 183
- Sault, R. J., Teuben, P. J., & Wright, M. C. H. 1995, in *Astronomical Society of the Pacific Conference Series*, Vol. 77, *Astronomical Data Analysis Software and Systems IV*, ed. R. A. Shaw, H. E. Payne, & J. J. E. Hayes, 433
- Scott, K. S., Austermann, J. E., Perera, T. A., et al. 2008, *MNRAS*, 385, 2225
- Scoville, N. Z., Carlstrom, J. E., Chandler, C. J., et al. 1993, *PASP*, 105, 1482
- Shimajiri, Y., Kawabe, R., Takakuwa, S., et al. 2011, *PASJ*, 63, 105
- Takakuwa, S., Saito, M., Lim, J., et al. 2012, *ApJ*, 754, 52
- Tobin, J. J., Hartmann, L., Chiang, H.-F., et al. 2012, *ArXiv e-prints*

Tsukagoshi, T., Saito, M., Kitamura, Y., et al. 2011, *ApJ*, 726, 45

Whitney, B. A., Wood, K., Bjorkman, J. E., & Cohen, M. 2003, *ApJ*, 598, 1079

Wilson, G. W., Auermann, J. E., Perera, T. A., et al. 2008, *MNRAS*, 386, 807

Wilson, T. L., & Rood, R. 1994, *ARA&A*, 32, 191

Wu, J., Dunham, M. M., Evans, II, N. J., Bourke, T. L., & Young, C. H. 2007, *AJ*, 133,
1560

Wu, P.-F., Takakuwa, S., & Lim, J. 2009, *ApJ*, 698, 184

Zhou, S., Evans, II, N. J., Koempe, C., & Walmsley, C. M. 1993, *ApJ*, 404, 232

Table 1. Parameters for the ASTE observations

Telescope/Receiver	ASTE/AzTEC	ASTE/CATS345	ASTE/CATS345	ASTE/CATS345
Line/Frequency/Wavelength	1.1 mm	$^{12}\text{CO}(J=3-2; 345.796 \text{ GHz})$	$\text{HCO}^+(J=4-3; 356.734 \text{ GHz})$	$\text{H}^{13}\text{CO}^+(J=4-3; 346.998 \text{ GHz})$
Observation date	2008 Oct 17 - 31	2011 May 30 - Jun 1	2011 May 30 - Jun 1, 2012 January 23	2012 January 23
Observing mode	Raster	OTF/Position switch	Position Switch	Position Switch
Mapping size	$35' \times 35'$	$15' \times 11' \& 80'' \times 80''$	$80'' \times 80'' \& 60'' \times 60''$	$60'' \times 60''$
Effective beam size	$36''$	$27''(\text{OTF}) / 22''(\text{Position Switch})$	$22''$	$22''$
Velocity resolution	–	0.10 km s^{-1}	0.11 km s^{-1}	0.10 km s^{-1}
Typical rms in T_{A}^*	7 mJy beam^{-1}	0.36 K	0.1 K & 0.03 K	0.03 K

Table 2. Parameters for the SMA data reductions

Line/Wavelength	1.3 mm	$^{12}\text{CO}(J=2-1)$	$^{13}\text{CO}(J=2-1)$	$\text{C}^{18}\text{O}(J=2-1)$
Frequency(GHz)	220.5 & 230.5	230.538	220.399	219.560
Observation date	2008 Mar 25			
Array Configuration	Compact (7 ant, Minimum Baseline=7 k λ , Maximum Baseline=50 k λ)			
Bandwidth / Channel Separation	2.0 + 2.0 GHz	1.1 km s $^{-1}$	1.1 km s $^{-1}$	1.1 km s $^{-1}$
Pointing Center	$(\alpha_{\text{J2000}}, \delta_{\text{J2000}})=(17^{\text{h}}11^{\text{m}}23^{\text{s}}.18, -27^{\circ}24'31''.5)$			
On Source Time	14 min			
System Temperature	80 - 130 K in SSB			
Bandpass Calibrators	3C454.3			
Complex Gain Calibrator	NRAO530, J1924-292			
Absolute Flux Calibrators	Callisto			
Beam Size	5''0 \times 2''8 (31)	4''8 \times 2''8 (31)	4''8 \times 2''9 (30)	5''2 \times 2''9 (32)
map rms	12 mJy beam $^{-1}$	200 mJy beam $^{-1}$	200 mJy beam $^{-1}$	200 mJy beam $^{-1}$

Table 3. Parameters of AzTEC/ASTE 1.1 mm dust-continuum condensations associated with YSOs

ID ^a	Spectrum ^a Type	α_{J2000}	β_{J2000}	Peak Flux Density [Jy beam ⁻¹]	Integrated Flux Density [Jy]	Source Size ["×"(P.A.°)]	Beam Deconvolve Size ["×"(P.A.°)]	Mass ^b [M _⊙]	Density [×10 ⁶ cm ⁻³]	Separation from Protostars ^e ["]
1 ^c	Flat	17:11:04.08	-27:22:57.0	0.26	0.26	36×34(58)	... ^c	0.37	0.98 ^d	3.1
3 ^d	I	17:11:12.46	-27:27:00.1	0.07	0.2	73×15(-28)	64×52	0.35	0.20	11
7 ^d	Flat	17:11:17.60	-27:25:16.2	0.11	0.2	60×44(0)	48×27	0.34	0.81	9.3
9	Flat	17:11:21.52	-27:27:40.5	0.28	0.3	46×42(-14)	... ^c	0.43	1.0 ^d	1.8
10	I	17:11:21.50	-27:26:11.7	0.44	1.1	76×51(55)	63×25	1.6	2.9	13
11	0/ I	17:11:23.22	-27:24:35.6	1.3	1.3	41×38(-63)	... ^c	0.09 ^f	1.9 ^g	4.2
14	I	17:11:25.21	-27:25:36.2	0.4	1.8	110×52(14)	103×39	2.5	0.65	29
(SMA)										
11 ^e	0/ I	17 11 23.08	-27 24 33.8	0.43	0.60	5.56×3.49 (22)	2.8×1.4 (-11)	0.015	2.7×10 ³ ^g	—

^aFrom Brooke et al. (2007).

^bEstimated on the assumption of $T_d=10$ K (Rathborne et al. 2008), $\kappa_\nu = 0.1(250\mu\text{m}/\lambda)^\beta \text{ cm}^2 \text{ g}^{-1}$ (Hildebrand 1983), and $\beta=2$.

^cThese dust-continuum sources are strongly suggested to be unresolved, and we cannot obtain the deconvolved sizes.

^dLower limits obtained using a beam size of 36".

^eSeparations between the peak positions of AzTEC/ASTE 1.1 mm dust-continuum condensations and protostars identified by Brooke et al. (2007).

^fEstimated on the assumption of $T_d=30$ K and $\beta=1.0$. See Section 3.1.1 in the text.

^gEstimated using the deconvolved size of 18"×17" obtained by Román-Zúñiga et al. (2012) from MAMBO-II 1.2 mm observations.

Table 4. Outflow Parameters

		Velocity [km s ⁻¹] ^a	Total Integrated Intensity	Mass [M _⊙] ^b	Energy [M _⊙ · (km s ⁻¹) ²] ^c	Momentum [M _⊙ · (km s ⁻¹)] ^c
ASTE	blue	-2.5~1.5	55 K·km s ⁻¹	9.5×10 ⁻³	1.3×10 ⁻¹	0.89
	red	5.5~9.5	120 K·km s ⁻¹	2.0×10 ⁻²	2.1×10 ⁻¹	1.2
SMA	blue	-5.0~1.5	36 Jy·km s ⁻¹	<2.8×10 ⁻⁴	<4.0×10 ⁻³	<3.0×10 ⁻²
	red	4.5~12	67 Jy·km s ⁻¹	<4.4×10 ⁻⁴	<3.4×10 ⁻³	<1.6×10 ⁻²

^aThe velocity ranges where emissions are detected above the 3 σ level.

^bMasses are estimated on the assumption of optically thin emission, $T_{\text{ex}}=10$ K, and $X[\text{CO}] = 10^{-4}$.

^cValues are estimated on the assumption of $i=75^\circ$ and $V_{\text{sys}} = 3.6$ km s⁻¹.

Table 5. Masses in HCO⁺ and H¹³CO⁺(4-3) emissions

Line		-1.5~2 km s ⁻¹	2~4 km s ⁻¹	5~8 km s ⁻¹	Total
HCO ⁺ (4-3)	integrated intensity (K(T_A^*)·km s ⁻¹)	0.28	2.5	0.41	3.2
	mass (M_\odot) ^a	1.2×10^{-2}	...	1.8×10^{-2}	3.0×10^{-2}
H ¹³ CO ⁺ (4-3)	integrated intensity (K(T_A^*)·km s ⁻¹)	...	0.17	...	
	mass (M_\odot) ^a	...	0.53	...	0.53

^aMasses are estimated on the assumption of optically thin emission, $T_{\text{ex}} = 30$ K, $X[\text{HCO}^+] = 1.0 \times 10^{-10}$, and $X[\text{H}^{13}\text{CO}^+] = 1.4 \times 10^{-12}$.

Table 6. Results of χ^2 -fitting

	Coefficient (a) ^a	Power-law index (b) ^a	Systemic velocity (v_{sys}) ^a	$\sqrt{\chi^2}$
$^{13}\text{CO}(2-1)$	4.4	-1.3	3.3	1.1
$\text{C}^{18}\text{O}(2-1)$	2.5	-0.61	3.3	1.1×10^{-1}
$\text{C}^{18}\text{O}(2-1)$	2.2	-0.5	3.3	6.8×10^{-1}
(fixed on Keplerian rotation)	$0.73 M_{\odot}$ ^b			

^a $|v_{\text{LSR}} - v_{\text{sys}}| = a \times r^b$ and r is the separation of a peak position with the 1.3 mm dust-continuum peak.

^bThe central stellar mass estimated from the fitting with a Keplerian rotation curve assuming the inclination angle of 75° .

Table 7. Results of SED fitting

Parameter	Edge-on	Riaz et al. (2009)
R_* (R_\odot)	5.6	3.4
T_* (K)	4000	3300
M_* (M_\odot)	0.81	0.28
θ_{in}	75°	53° - 59°
$R_{\text{env,max}}$ (AU)	3000	4000
$R_{\text{disk,max}}$ (AU)	390	30
M_{disk} (M_\odot)	7.0×10^{-3}	2.6×10^{-2}

Table 8. Comparison with L1551NE

Parameter	B59#11	L1551NE
$L_{\text{bol}} (L_{\odot})$	2.0	4.2
$T_{\text{bol}} (\text{K})$	70	91
$R_{\text{disk}} (\text{AU})$	<350	300
$M_{*} (M_{\odot})$	0.84	0.8
$M_{\text{disk}} (M_{\odot})$	0.016	0.015
$R_{\text{env}} (\text{AU})$	2300 ^a	>8500 ^b
$M_{\text{env}} (M_{\odot})$	0.082	0.24
specific angular momentum ($\text{km s}^{-1} \text{ pc}$)	1.9×10^{-3}	6×10^{-4}

^aThe deconvolved size obtained from IRAM/MAMBO-II 1.2 mm continuum observations (Román-Zúñiga et al. 2012)

^bThe size of the sharp edge of the density profile obtained from IRAM/MPIFR 1.3 mm continuum observations (Motte & André 2001)

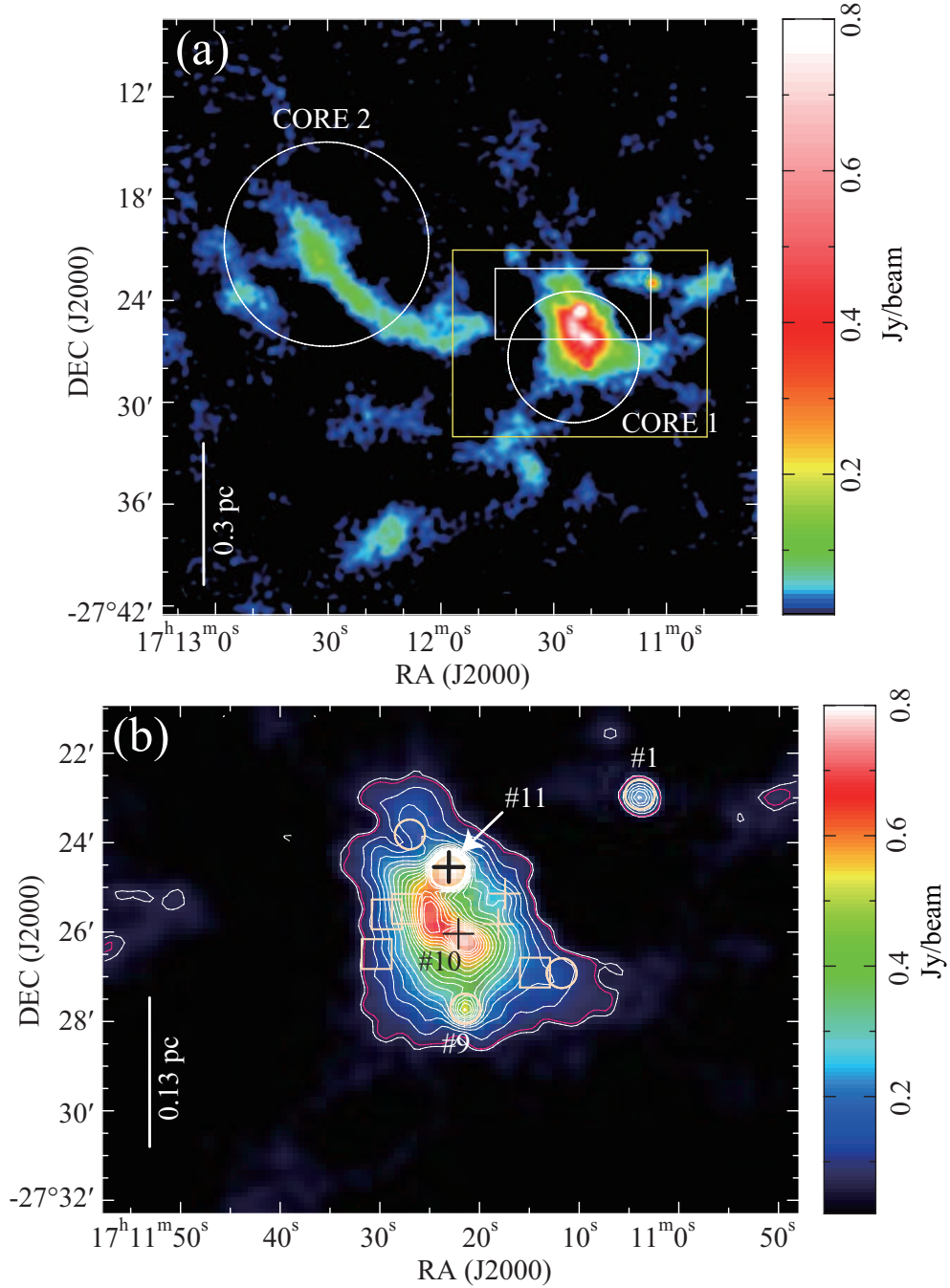


Fig. 1.— AzTEC/ASTE 1.1 mm dust-continuum map. The white box shows the area of Figure 3, and the yellow box shows the observing area of ASTE CO(3–2) emission (Figure 4). Contour levels start at 3σ noise level with an interval of 6σ ($1\sigma=7$ mJy beam⁻¹). The B59 mass is derived from emission within the pink contour ($\geq 10\sigma$) (Section 3.1.1). The crosses, circles, and boxes show positions of Class-I, flat, and Class-II YSOs, respectively (Forbrich et al. 2009). The white circles in (a) show the locations and the extents of Core 1 and Core 2 identified by Onishi et al. (1999)

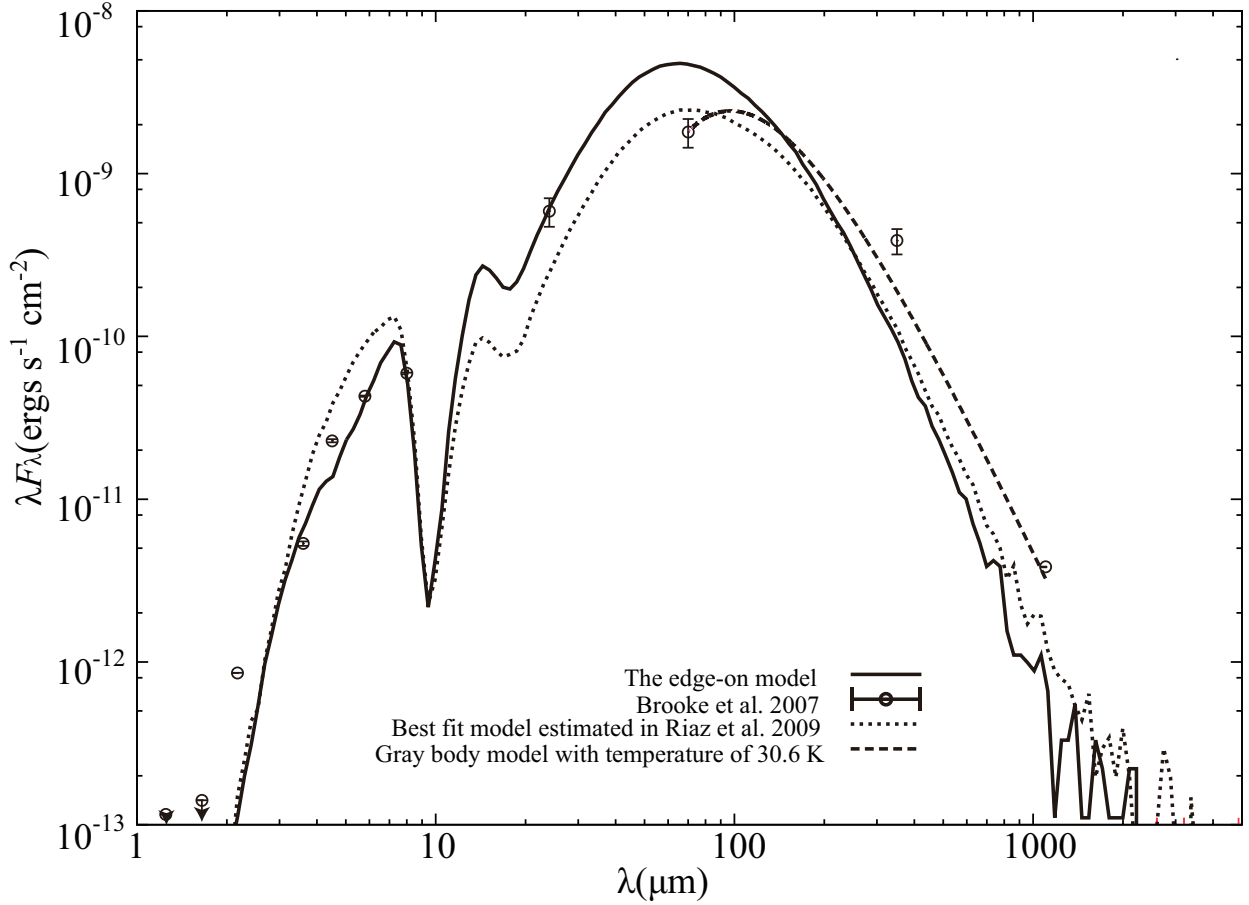


Fig. 2.— Spectral energy distribution (SED) of B59#11. The flux densities of infrared emissions are from Brooke et al. (2007), and that of the 350 μm emission is from the results of SHARC-II observations (Wu et al. 2007). We used the two-dimensional radiative transfer code by Whitney et al. (2003) and the SED fitting tool by Robitaille et al. (2007). The solid line shows the edge-on protostellar model and the dotted line shows the model fitted by Riaz et al. (2009). The dashed line shows the graybody model with a temperature of 30.6 K and $\beta = 1$.

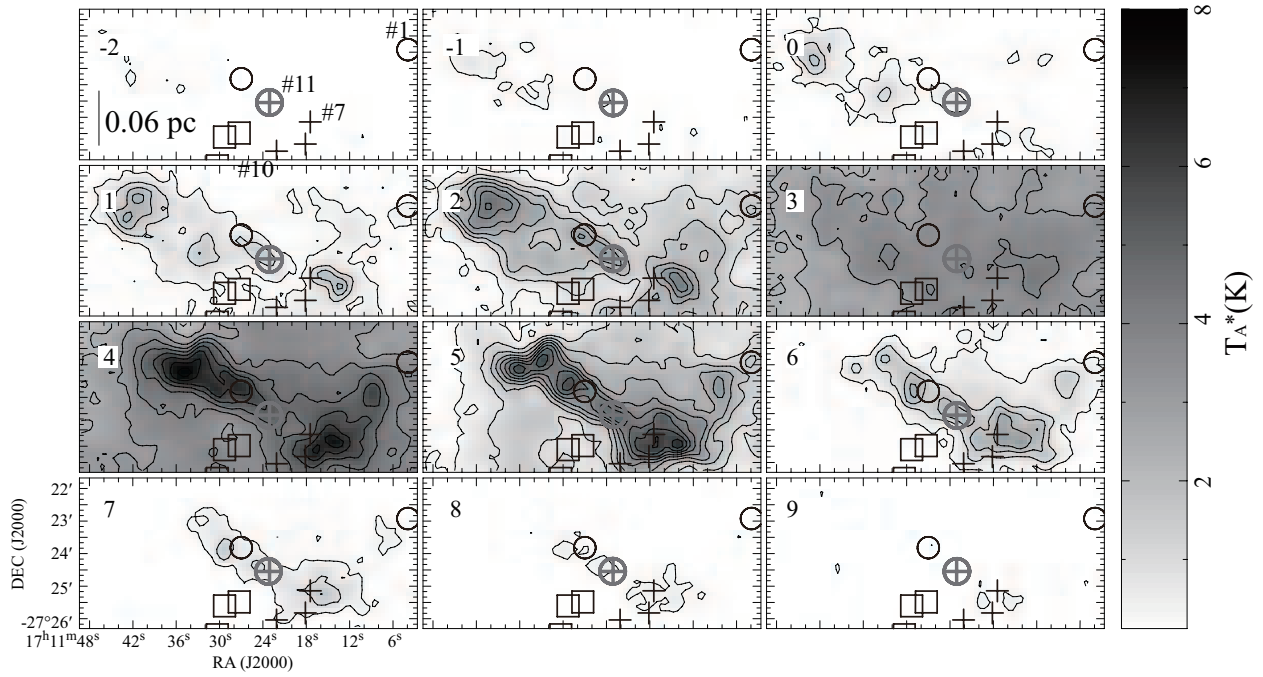


Fig. 3.— Velocity channel maps of ASTE CO(3–2) emission with the velocity range of -2-9 km s⁻¹. Contour levels start at 3 σ noise level with an interval of 3 σ ($1\sigma=0.2$ K(T_A^*)). The symbols are the same as those in Figure. 1. The gray circles around B59#11 is the SMA FoV.

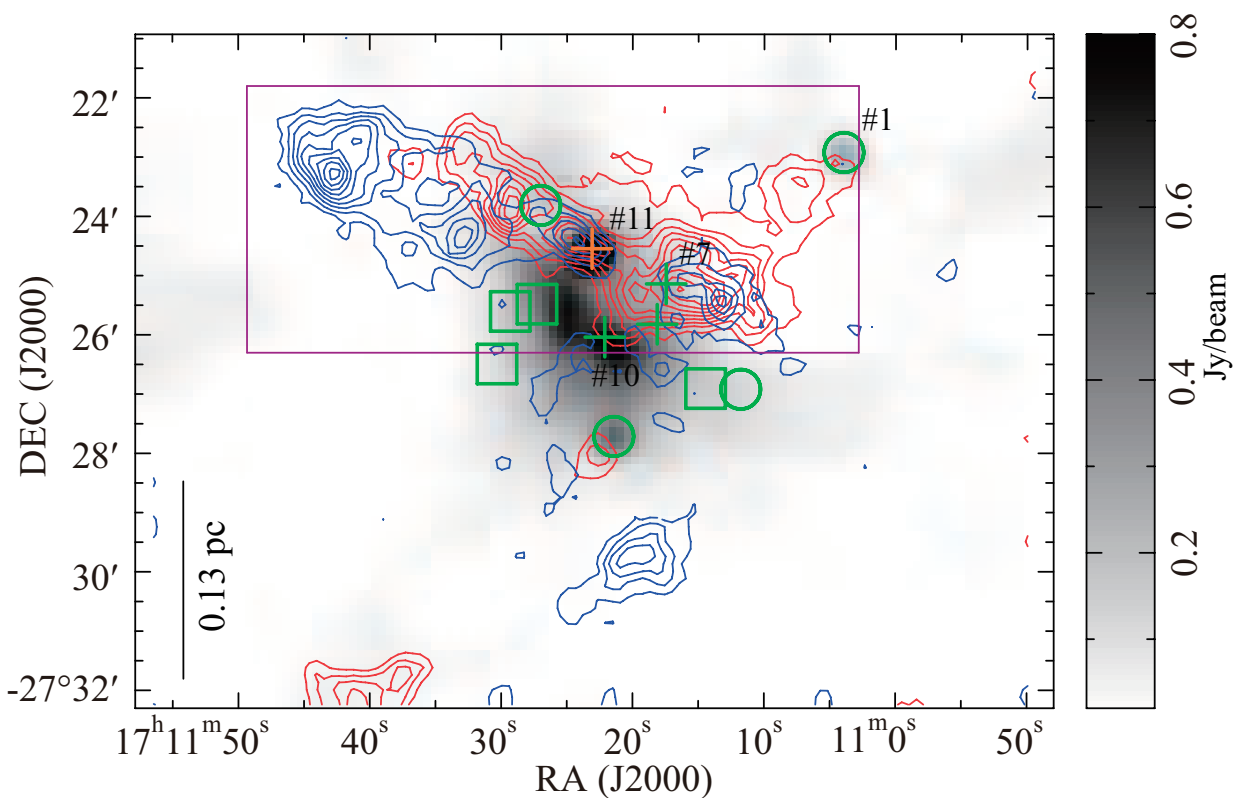


Fig. 4.— ASTE CO(3–2) map of the B59 overlaid on the AzTEC/ASTE 1.1 mm dust-continuum image. The blue and red contours represent blueshifted and redshifted CO(3–2) intensities integrated between $V_{\text{LSR}} = -2.5$ to 1.5 km s^{-1} and 5.5 to 9.5 km s^{-1} , respectively. Contour levels start at 3σ noise level with an interval of 2σ ($1\sigma=0.3 \text{ K}(T_{\text{A}}^*) \cdot \text{km s}^{-1}$). The symbols are the same as those in Figure 1. The purple box shows the area of Figure 3.

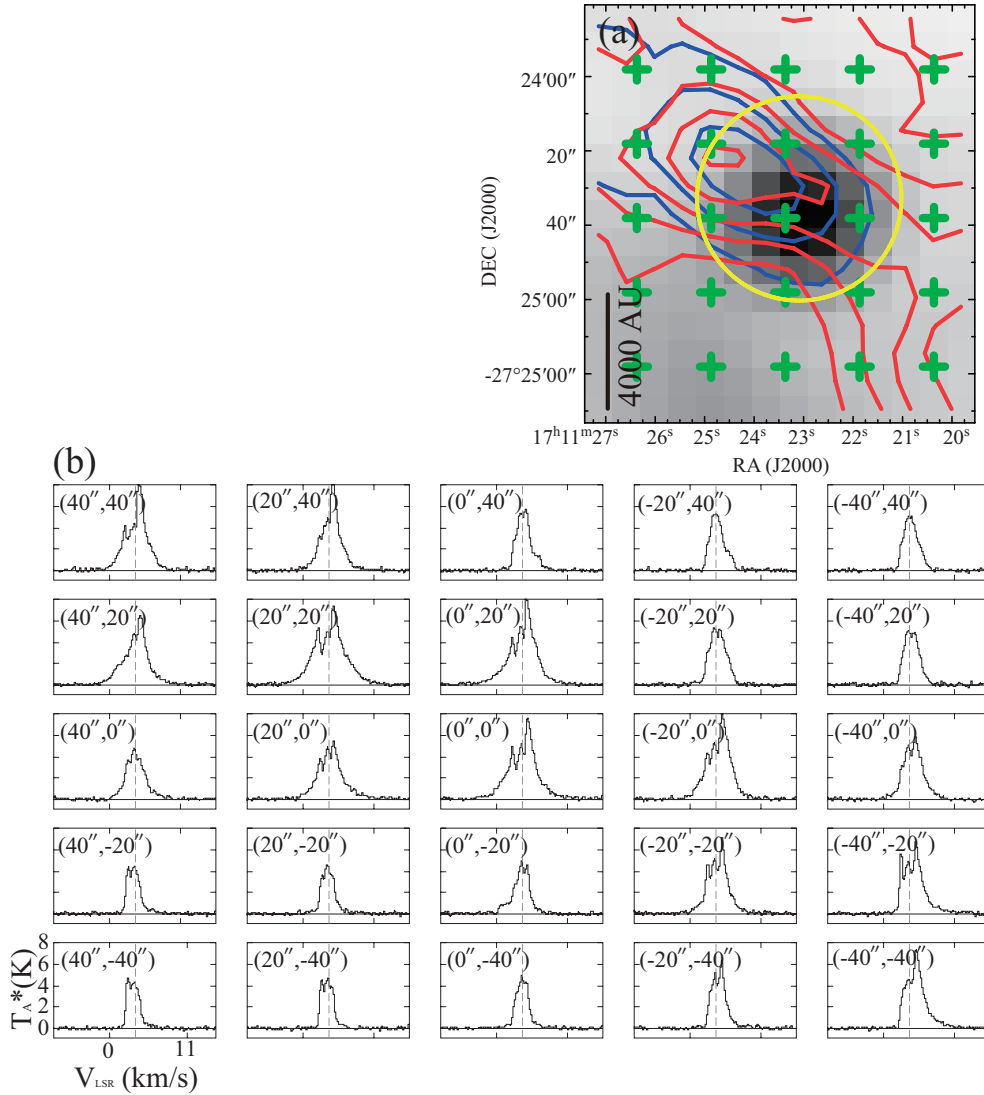


Fig. 5.— (a) CO(3–2) map (the same as Figure 4), and (b) CO(3–2) profile map taken toward B59#11. The green crosses in Figure (a) show the positions where profiles in Figure (b) were obtained, and the yellow circle shows the SMA FoV. A grid spacing of Figure (b) is 20''. The dotted vertical lines are the systemic velocity of 3.6 km s⁻¹ obtained from ASTE H¹³CO⁺(4–3) observations (Figure 6). The (0'', 0'') position is the peak position of AzTEC/ASTE 1.1 mm dust-continuum condensation associated with B59#11, ($\alpha_{J2000.0}, \delta_{J2000.0}$) = (17^h11^m23^s.1, -27°24'38".2).

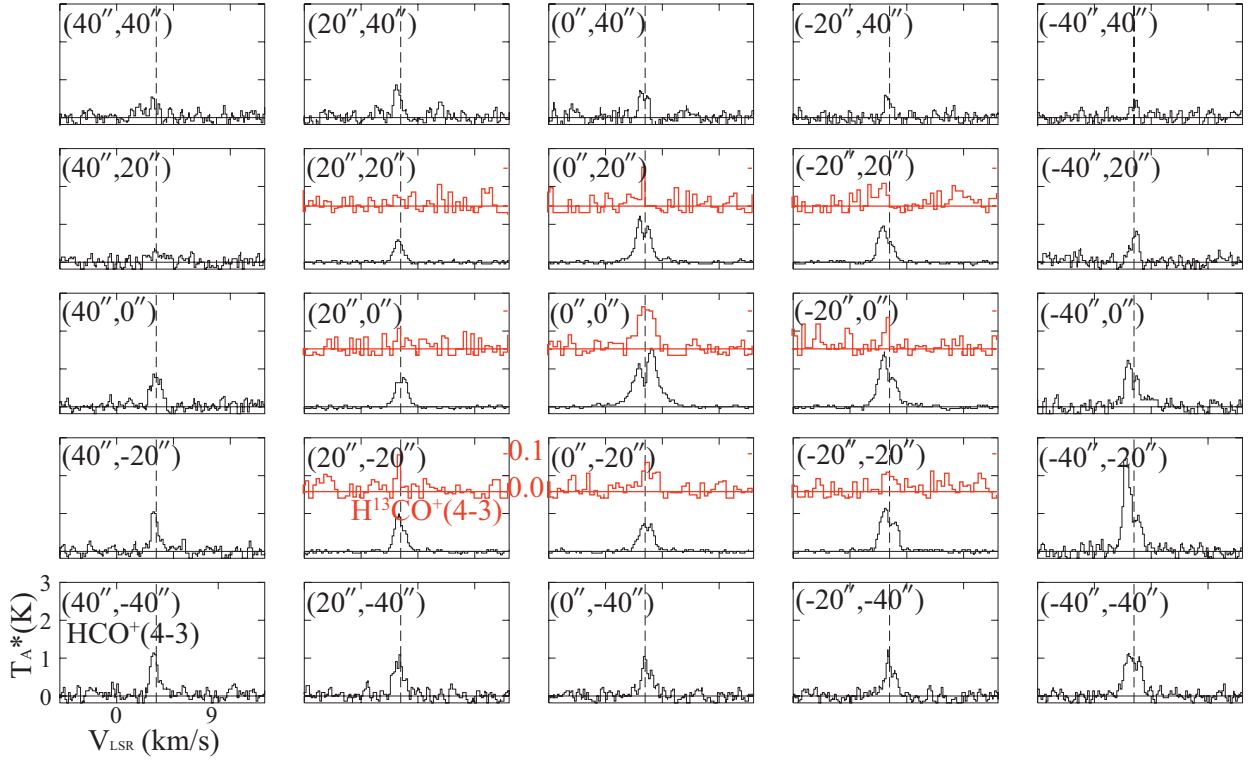


Fig. 6.— ASTE $\text{HCO}^+(4-3)$ (black lines) and $\text{H}^{13}\text{CO}^+(4-3)$ (red lines) profile maps. The dotted vertical lines are the systemic velocity. The $(0'', 0'')$ position and a grid spacing is the same as those of Figure 5 (b).

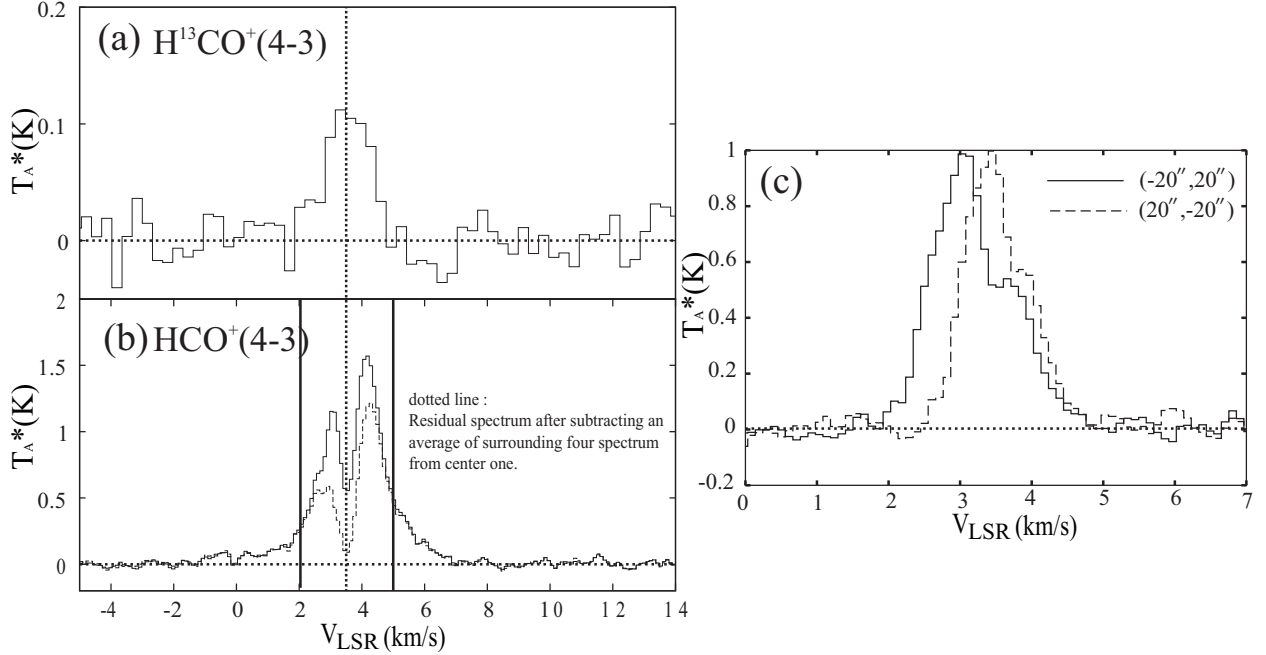


Fig. 7.— The profiles of (a) $\text{H}^{13}\text{CO}^+(4-3)$ and (b) $\text{HCO}^+(4-3)$ lines at the $(0'', 0'')$ position in Figure 6. The dotted line in Figure (b) shows the residual spectrum after subtracting an average of surrounding four spectra from that at the center. The dotted vertical lines are the systemic velocity and the solid vertical lines in (b) indicate the velocity range where the masses of the high velocity components are obtained (Table 5). (c) Line profiles of $\text{HCO}^+(4-3)$ at the positions of $(-20'', 20'')$ and $(20'', -20'')$.

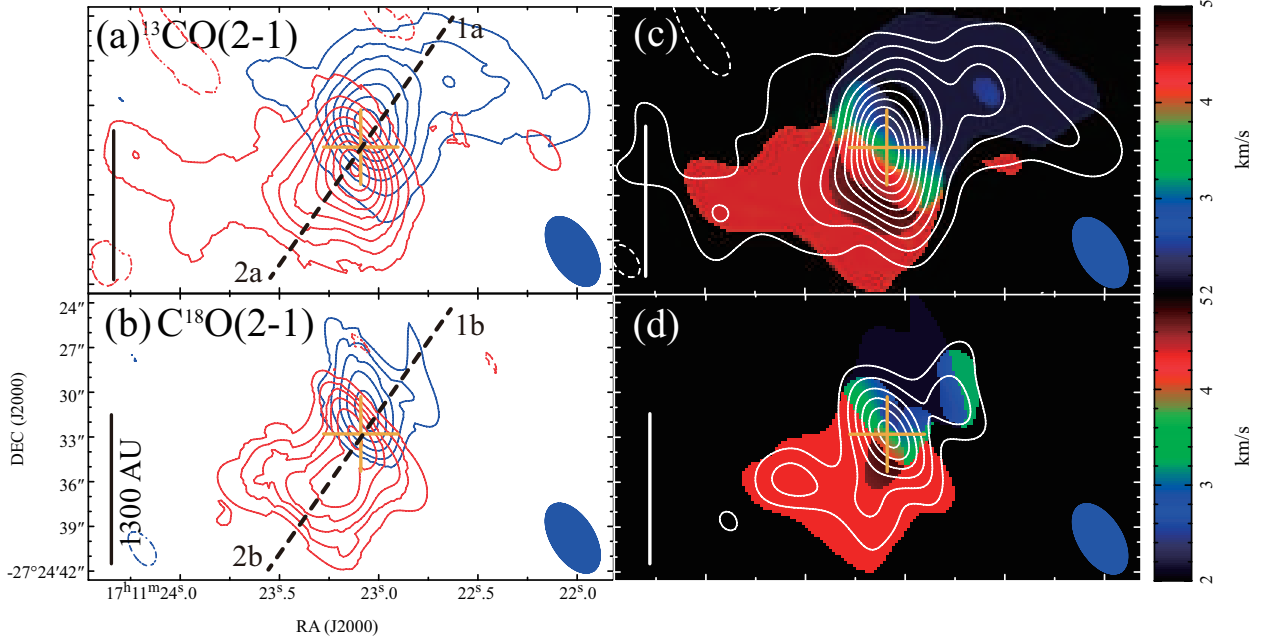


Fig. 8.— The maps of (a) (c) SMA $^{13}\text{CO}(2-1)$ and (b) (d) $\text{C}^{18}\text{O}(2-1)$ emissions. The blue and red contours represent blueshifted and redshifted intensities integrated between (a) $V_{\text{LSR}} = -0.5$ to 1.2 km s^{-1} and 3.9 to 8.2 km s^{-1} , and (b) 0.5 to 2.6 km s^{-1} and 3.8 to 8.2 km s^{-1} , respectively. The white contours superposed on the mean velocity maps in (c) and (d) indicate the emissions integrated over intervals from $V_{\text{LSR}} = -0.5$ to 8.2 km s^{-1} , and from 0.5 to 8.2 km s^{-1} . Contour levels start at 3σ noise level with intervals of (a) 3σ ($1\sigma = 0.5 \text{ Jy beam}^{-1} \text{ km s}^{-1}$), (b) 1.5σ ($1\sigma = 0.3 \text{ Jy beam}^{-1} \cdot \text{km s}^{-1}$), (c) 3σ ($1\sigma = 0.6 \text{ Jy beam}^{-1} \cdot \text{km s}^{-1}$), and (d) 1.5σ ($1\sigma = 0.6 \text{ Jy beam}^{-1} \cdot \text{km s}^{-1}$). The blue ellipses at the bottom-right corners show the beam size, and the crosses indicate the position of B59#11 (Forbrich et al. 2009). The dashed lines in (a) and (b) indicate the cuts along which the P-V diagrams in Figure 11 (a) and (b) were produced.

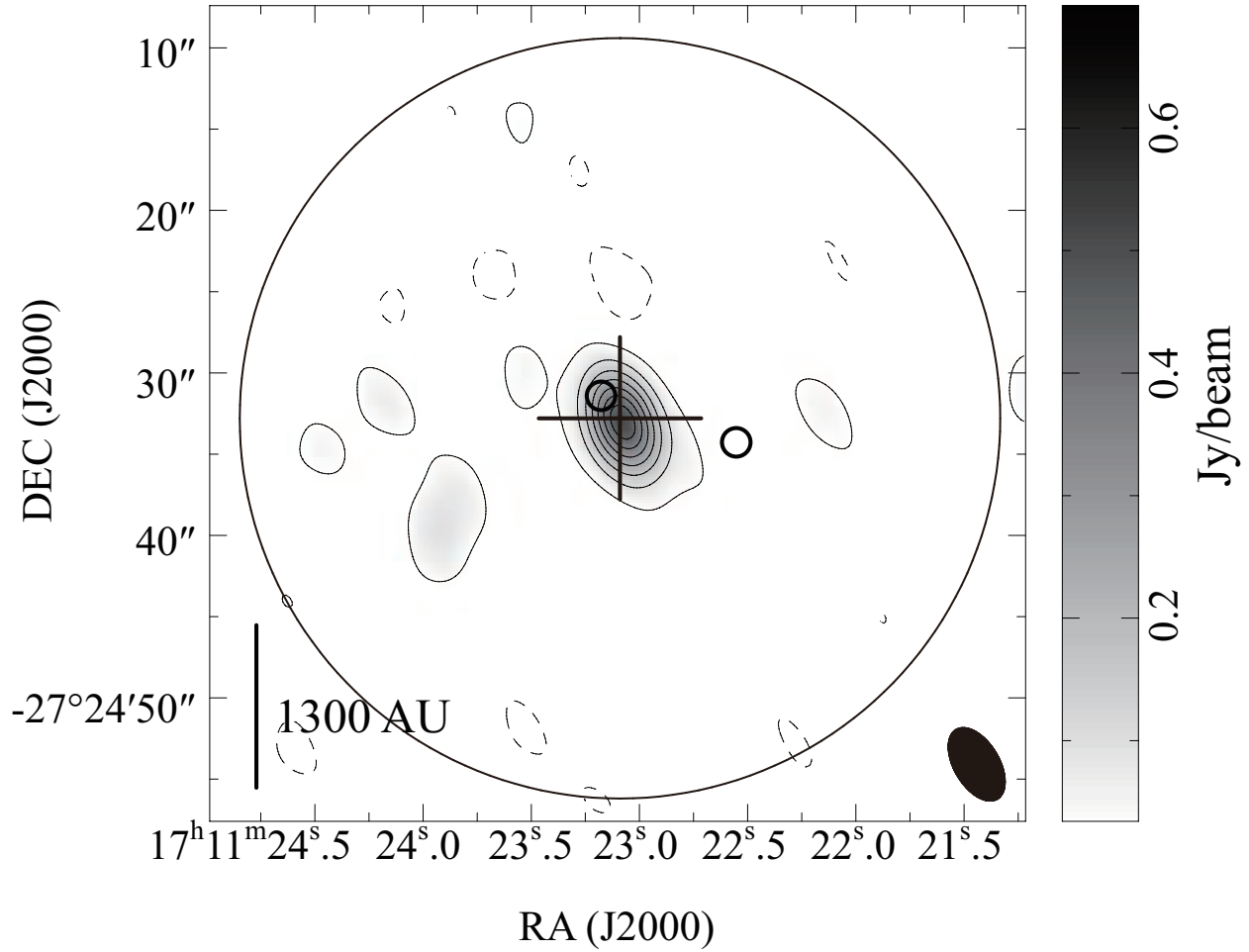


Fig. 9.— SMA 1.3 mm dust-continuum map. Contour levels are start at 3σ noise level with intervals of 6σ ($1\sigma=0.012$ Jy beam $^{-1}$). The small circles show the positions of B59#11 and B59#11SW which are identified with the infrared observations (Riaz et al. 2009). The big circle shows the SMA FoV of $54''$. The other symbols are the same as those in Figure 8.

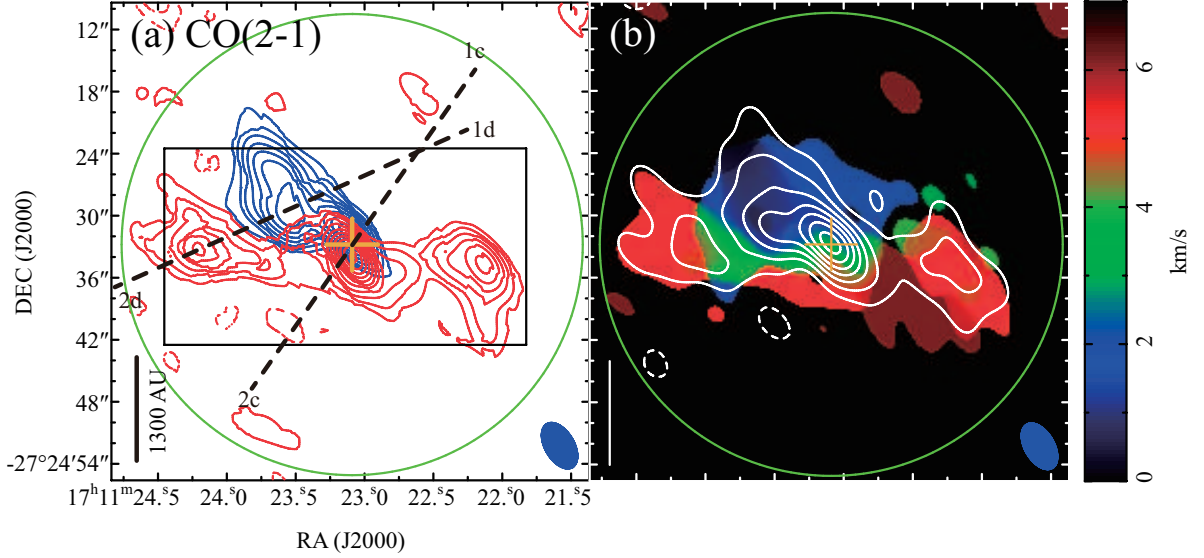


Fig. 10.— The maps of SMA CO(2-1) emission. The blue and red contours represent blueshifted and redshifted intensities integrated between $V_{\text{LSR}}=-4.9$ to 1.4 km s^{-1} and 4.6 to 12 km s^{-1} , respectively. The white contours superposed on the mean velocity map in (b) indicate the emission integrated over intervals from $V_{\text{LSR}}=-4.9$ to 12 km s^{-1} . Contour levels start at 3σ noise level with intervals of (a) 1.5σ ($1\sigma=1.0 \text{ Jy beam}^{-1}\cdot\text{km s}^{-1}$), and (b) 3σ ($1\sigma=1.8 \text{ Jy beam}^{-1}\cdot\text{km s}^{-1}$). The symbols in each figure are the same as those in Figure 9. The dashed lines in (a) are cuts along which the P-V diagrams in Figure 11 (c) and (d) were produced.

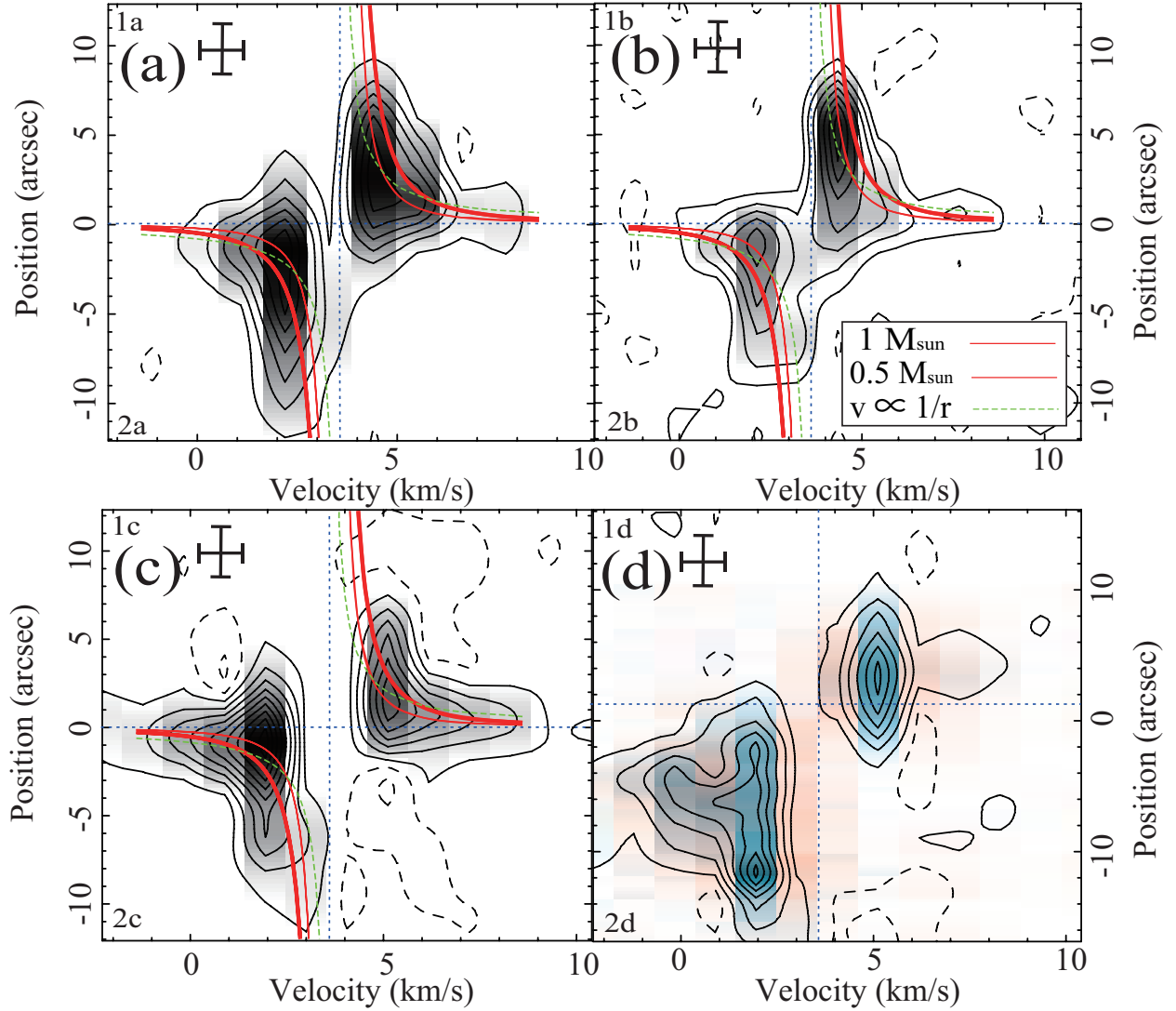


Fig. 11.— Position-Velocity diagrams in (a) SMA $^{13}\text{CO}(2-1)$, (b) $\text{C}^{18}\text{O}(2-1)$, and (c) (d) $\text{CO}(2-1)$ emissions, cut along lines with a PA of 145° centered at B59#11 (Figure 8, 10). Contour levels are start at (a) (c) (d) 3σ and (b) 1.5σ noise level with intervals of (a) 3σ ($1\sigma=0.2 \text{ Jy beam}^{-1}$), (b) 1.5σ ($1\sigma=0.2 \text{ Jy beam}^{-1}$), and (c) (d) 6σ ($1\sigma=0.2 \text{ Jy beam}^{-1}$), respectively. The blue dashed lines in the vertical and horizontal directions show the systemic velocity and the position of B59#11. The red thick and narrow lines show Keplerian disk models for the central masses of $1.0 M_\odot$ and $0.5 M_\odot$, and the green curves show the rotation conserving its angular momentum ($r \propto v^{-1}$) whose rotation velocity is 2 km s^{-1} at a radius of 200 AU.

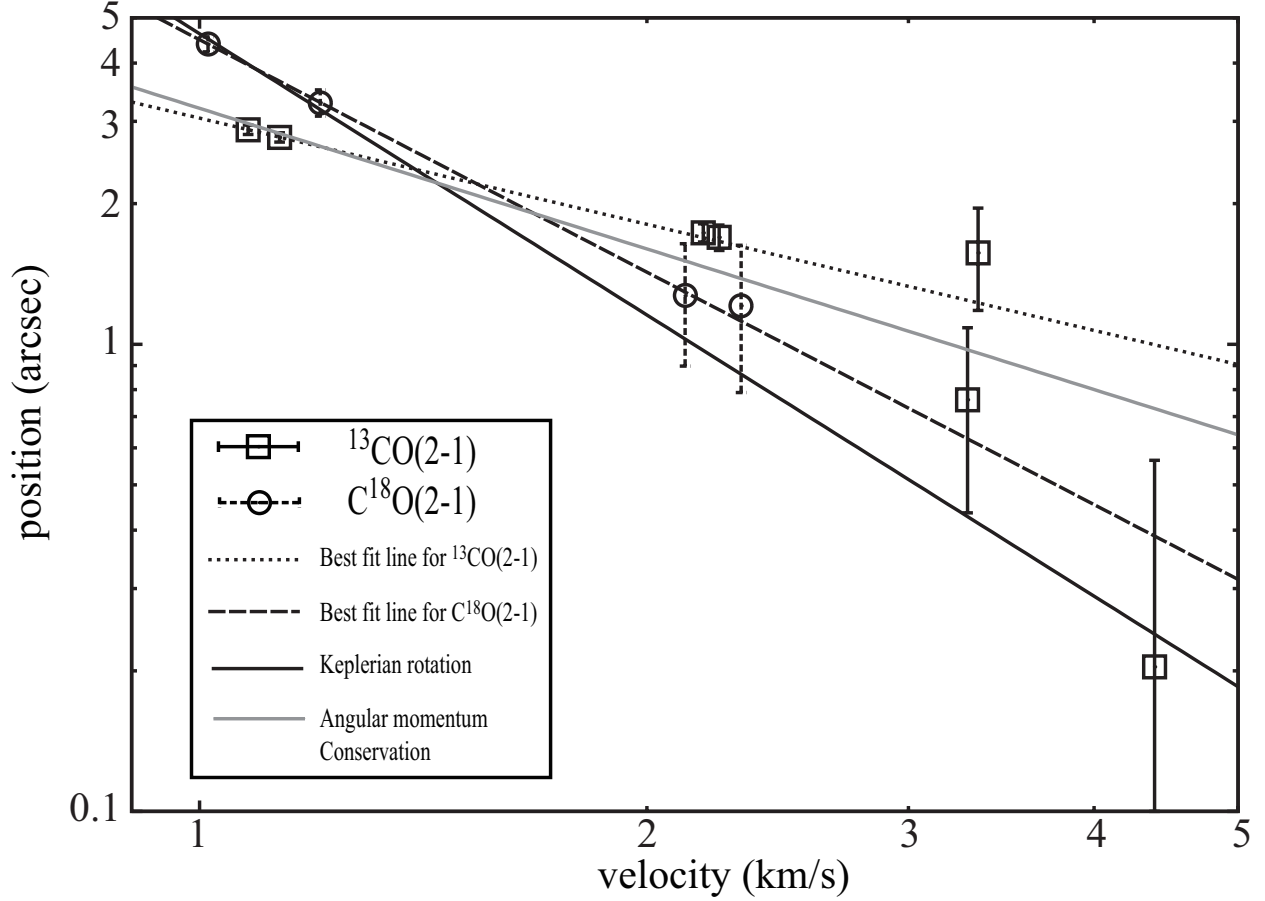


Fig. 12.— Logarithmic plot of the measured radius as a function of velocities. The boxes and circles show separations of the positions between 1.3 mm dust-continuum peak and $^{13}\text{CO}(2-1)$ and $\text{C}^{18}\text{O}(2-1)$ peaks in each velocity channel. The dotted line shows the best fit line for $^{13}\text{CO}(2-1)$ emission ($v \propto r^{-1.3}$) and the long-dashed line shows the best fit line for $\text{C}^{18}\text{O}(2-1)$ emission ($v \propto r^{-0.61}$). The black solid line shows the Keplerian rotation with a central stellar mass of $0.73 M_{\odot}$ fitted for $\text{C}^{18}\text{O}(2-1)$ emission, and the gray solid line shows the rotation conserving its angular momentum of $2.1 \times 10^{-3} \text{ km s}^{-1} \text{ pc}$.